A hybrid discrete-continuum model of immune responses to SARS-CoV-2 infection in the lung alveolar region, with a focus on interferon induced innate response

Andreas C. Aristotelous [a,*], Alex Chen [b,1], M. Gregory Forest [c,2]

[a] Department of Mathematics, The University of Akron, Akron, OH 44325-4002, United States of America
[b] Department of Mathematics, California State University, Dominguez Hills, CA 90747, United States of America
[c] Departments of Mathematics, Applied Physical Sciences, and Biomedical Engineering, University of North Carolina at Chapel Hill, Chapel Hill, NC 27599-3250, United States of America

ARTICLE INFO

Keywords:
COVID-19
Simulations
Cellular automaton
Innate immunity
Pneumonia

ABSTRACT

We develop a lattice-based, hybrid discrete-continuum modeling framework for SARS-CoV-2 exposure and infection in the human lung alveolar region, or parenchyma, the massive surface area for gas exchange. COVID-19 pneumonia is alveolar infection by the SARS-CoV-2 virus significant enough to compromise gas exchange. The modeling framework orchestrates the onset and progression of alveolar infection, spatially and temporally, beginning with a pre-immunity baseline, upon which we superimpose multiple mechanisms of immune protection conveyed by interferons and antibodies. The modeling framework is tunable to individual profiles, focusing here on degrees of innate immunity, and to the evolving infection–replication properties of SARS-CoV-2 variant strains. The model employs partial differential equations for virion, interferon, and antibody concentrations governed by diffusion in the thin fluid coating of alveolar cells, species and lattice interactions corresponding to sources and sinks for each species, and multiple immune protections signaled by interferons. The spatial domain is a two-dimensional, rectangular lattice of alveolar type I (non-infectable) and type II (infectable) cells with a stochastic, species-concentration-governed, switching dynamics of type II lattice sites from healthy to infected. Once infected, type II cells evolve through three phases: an *eclipse phase* during which RNA copies (virions) are assembled; a *shedding phase* during which virions *and* interferons are released; and then *cell death*. Model simulations yield the dynamic spread of, and immune protection against, alveolar infection and viral load from initial sites of exposure. We focus in this paper on model illustrations of the diversity of outcomes possible from alveolar infection, first absent of immune protection, and then with varying degrees of four known mechanisms of interferon-induced innate immune protection. We defer model illustrations of antibody protection to future studies. Results presented reinforce previous recognition that interferons produced solely by infected cells are insufficient to maintain a high efficacy level of immune protection, compelling additional mechanisms to clear alveolar infection, such as interferon production by immune cells and adaptive immunity (e.g., T cells). This manuscript was submitted as part of a theme issue on "Modelling COVID-19 and Preparedness for Future Pandemics".

1. Introduction

The COVID-19 pandemic has had a devastating worldwide impact that continues at this writing. The pandemic has and will continue to have many long lasting effects, yet one lesson learned is the essential need for detailed scientific understanding of infection from respiratory viruses with sufficient fidelity to inform medical and public health responses. Clearly, our understanding of the science of respiratory infections from a novel coronavirus was woefully insufficient. The scientific community has responded with a full-scale effort since early 2020 to identify and fill the many gaps in understanding of exposure

* Corresponding author.
E-mail addresses: aaristotelous@uakron.edu (A.C. Aristotelous), achen@csudh.edu (A. Chen), forest@unc.edu (M.G. Forest).

[1] The author was partially supported by CSUDH RSCA and NSF DMS-2028758.
[2] The author was partially supported by NSF DMS-1664645, CISE-1931516, DMS-1929298, DMS-2028758, and the North Carolina Policy Collaboratory at the University of North Carolina at Chapel Hill with funding from the North Carolina Coronavirus Relief Fund established and appropriated by the North Carolina General Assembly.

https://doi.org/10.1016/j.jtbi.2022.111293
Received 1 July 2022; Received in revised form 16 September 2022; Accepted 21 September 2022
Available online 5 October 2022

risks, and both within-host and host-to-host transmission of infection. The promises of rigorous understanding of respiratory infections from a novel virus are to inform the public of behavior for their and others' safety, to guide public policy, and to inform medical prevention and treatment. Mathematical modeling and simulation are key elements to each of these promises.

Mathematical modeling of host-to-host transmission of infection is one of the hallmark achievements of modeling, and adaptation of these modeling advances to the SARS-CoV-2 respiratory virus has had positive impacts on public communication and policy, as covered by other articles in this special issue. The focus of our paper is on *within-host respiratory infection*, a less developed and data-supported area of mathematical modeling of infectious disease for various reasons. One major roadblock to within-host modeling of respiratory viral exposure and infection is the egregious lack of data to validate or benchmark model predictions. Indeed, the primary human *in vivo* data is from nasal swab and sputum tests that are commonplace in the COVID-19 pandemic (Wölfel et al., 2020; Kissler et al., 2021). On the flip side, all human data on alveolar infections, the very condition that leads to pneumonia, hospitalization, and sometimes death, comes from donor human lungs. There is little possibility of *in vivo* human data on the progression of alveolar infection and the reaction and adaptation of the immune system to deep lung infection to arrest and eliminate infection. A few studies indicate that the worst clinical outcomes appear correlated with high alveolar viral loads (Blot et al., 2021) and heightened immune cell activity (Grant et al., 2021; Lv et al., 2021).

Thus, the available insights into the *dynamics* of human alveolar infection are provided by *ex vivo* cell cultures where donor alveolar tissue is grown and exposed to viruses (Hui et al., 2022), and inferences gained from primate studies (Goyal et al., 2022). Additionally, there are ongoing studies on the dynamics of infection in animal models, e.g., mice (Dinnon et al., 2020)and ferrets (Vaidya et al., 2021). Yet the pathology of COVID-19 alveolar pneumonia also has distinct characteristics in comparison with other pneumonia that warrant further study, such as its relatively slow progression and severe inflammatory response (Grant et al., 2021; Gattinoni et al., 2020; Bost et al., 2020; Zhou et al., 2020). However, without analogous data from human deep lung infection, the equivalence or lack thereof between *ex vivo* alveolar culture infection, animal models, and human parenchymal (alveolar) infection remains open, compelling the potential value of physiologically faithful, quantitative modeling of the dynamics of *in vivo* deep lung infection.

This gap in current and future possibility of *in vivo* data is our motivation to develop a focused modeling framework, or platform, for alveolar infection. The goal is to orchestrate: the physiology and anatomy of the alveolar space; the degrees (from absent to maximal) of innate and adaptive immune and other protective response mechanisms such as drugs to a target virus (here, SARS-CoV-2); the timing of protective responses or interventions relative to exposure and infection; and, infection–replication properties of the target virus (that have changed with new SARS-CoV-2 variants through numerous mutations Korber et al., 2020; Bar-On et al., 2020; Sender et al., 2021; Hui et al., 2022; Peacock et al., 2022; Jung et al., 2022). In Chen et al. (2022a), a stochastic spatial model of a novel viral exposure and infection in the respiratory tract, including the alveolar space, was developed. The model predicts outcomes of the spatial distribution and progression of infected cells and viral load from local, generation-specific, seeds of exposure, assuming the complete absence of immune protection in the immediate hours and days following exposure to a novel virus. In a companion submission (Chen et al., 2022b) to the present paper, the stochastic model is extended to include antibodies, and to explore the mechanisms of protection by antibodies at locations throughout the respiratory tract.

Here, we replace the stochastic model of individual virions, antibodies, and infectable alveolar type II cells with a hybrid continuum-stochastic model focusing exclusively on the alveolar space. This singular focus on the alveolar space is motivated by the result in Chen et al. (2022a) that *alveolar infection results from direct deposition of infectious virion seeds into the alveolar generations*, from which the seeds grow and spread. That is, alveolar infection does not arise from retrograde progression of infection from generations in the lower respiratory tract down to the lung parenchyma. Furthermore, many physically separated infectious seeds are necessary to infect a measurable percentage of the 140 square meters of alveolar epithelial surface area. Likely sources of seed depositions directly into the deep lung parenchyma are discussed in Chen et al. (2022a), with the primary source due to aspiration of infected nasal and pharyngeal fluid boluses. Experimental evidence for this self-infection pathway is given in Hou et al. (2020). An alternative deterministic ODE model of self-transmission along the "oral-lung aspiration axis" is given in Ke et al. (2021). We also call attention to the work by Pearson et al. (2011) and the powerful agent-based respiratory tract infection model SIMCoV (Moses et al., 2021). The daunting challenge of understanding respiratory exposure and infection compels multiple strategies, including those cited above and the present paper, for mathematical modeling and simulations that can evolve with and learn from experimental and clinical data, and from the strengths of each modeling strategy.

The present hybrid model of alveolar or parenchymal infection (without and with immune protection) consists of continuum partial differential equations governing the species concentrations of virions, antibodies, and interferons that diffuse and interact over a two-dimensional lattice of alveolar cells. Since the primary targets for infection are type II cells (Lamers and Haagmans, 2022), we assume that the lattice consists of uninfectable type I and infectable type II cells. Meanwhile, a stochastic model governs switching dynamics of type II cell lattice sites from uninfected to infected with a probability governed by virion concentration. Once infected, type II cells evolve deterministically between three phases: *a latency or eclipse phase* during which infectious RNA copies are assembled and replicated, set to a fixed duration between 2 h and 12 h that is conjectured in Pearson et al. (2022) to be the dominant mutational consequence of the SARS-CoV-2 variants; *a shedding phase* during which infectious RNA copies are released at a fixed, uniform shedding rate between 500 and 2000 per day for a fixed number of days between 3 and 5; finally, *cell death* with a possible replacement after some prescribed time by a healthy type II cell. The deterministic evolution of infected type II cells is further allowed to be interrupted by interferon-signaled macrophages that abruptly terminate the latency or shedding phases, or by interferon-signaled reduction in replication and shedding rate of infectious viral progeny. Another protection mechanism in the model is interferon-signaled immune cells (e.g., macrophages) that envelop infectious virions, modeled as a virion sink proportional to interferon concentration. Simulations of this coarse-grained alveolar infection model are first compared with pre-immunity results of the stochastic model (Chen et al., 2022a) and then implemented to explore immune protection scenarios for several presumed individual profile conditions and SARS-CoV-2 variant properties. For this study, we focus simulations exclusively on the direct and indirect mechanisms and ranges of innate immune protection provided by interferons.

2. The model

Our SARS-CoV-2 alveolar infection model incorporates the concentrations of infectious virions v, interferons (IFN) u, and antibodies (Ab) w, their transport properties, direct and implicit interactions, and their interactions with alveolar cells. We consider a square domain Ω and use a lattice-based model to represent the alveolar space where each lattice site $\mathbf{x}$ in the square lattice is either occupied by a healthy type II cell (in state 1, $\xi(\mathbf{x}) = 1$), an infected type II cell (in state 2, $\xi(\mathbf{x}) = 2$), a type I cell (in state 0, $\xi(\mathbf{x}) = 0$), or a dead (type II) cell (in state -1, $\xi(\mathbf{x}) = -1$). An infected type II cell has an "internal clock", which starts counting at $\tau = 0$ when the cell has just been infected; for $0 \leq \tau \approx \tau_1$ hours the virus reprograms the cell to assemble and replicate RNA copies of

itself, often termed the eclipse phase; for $\tau_1 \le \tau \approx \tau_2$, the infected cell sheds RNA copies into the alveolar fluid (we only track viable, infectious RNA copies, i.e., infectious virions) with rate λ, providing a virion source term; for $\tau \ge \tau_2$ the infected cell dies and ceases virion shedding. As discussed next, in the presence of immune protection triggered by interferons from the infected lattice site or nearby infected cells, this deterministic clock can be interrupted either by interferon-induced partial immunity (interference in cell infectability or in infected cell replication and shedding of infectious progeny) or by death of the infected cell by the action of interferon-signaled immune cells. The parameter values of λ, τ_1 and τ_2 are predicted in Pearson et al. (2022) to not only vary with, but to distinguish nasal infection outcomes from, the SARS-CoV-2 variants. Here we explore the impacts of these parameters on alveolar infection outcomes, explored recently in alveolar cell cultures (Hui et al., 2022).

Infected type II cells produce and release signaling molecules called interferons, a class of cytokines. Interferons signal both the infected cell and nearby cells, directly interfering with and limiting the ability of virions to infect those cells, and also signal nearby macrophages as well as other immune cells (macrophages, killer cells, T cells). We do not include adaptive immune protection by T cells in the present model. Once cells are infected, interferons also limit the assembly, replication, and shedding of infectious progeny McNab et al. (2015) and Iyer et al. (2017). Specifically, interferons signal neighboring epithelial cells to increase the numbers of class I major histocompatibility complex proteins (or MHC class I) on their surface, enabling immune cells (macrophages, killer cells) to identify and eliminate the infected cell via phagocytosis or other cytotoxic factors Hagemann et al. (2022). In our model interferons are released at a prescribed rate λ_u by infected cells in the shedding phase; since we do not model macrophages explicitly, this rate includes the potential source of interferons from macrophages. Considering infected type II cells and macrophages to be the primary IFN producers in the lung is supported by Swiecki and Colonna (2011) and Wang et al. (2009). Interferons trigger the following protection mechanisms proportional to interferon concentration: an infected type II cell occupying a lattice site has a probability of being eliminated by macrophages; virions are eliminated at a rate κv; type II cells are immunized (Domingo-Calap et al., 2019; Michael Lavigne et al., 2021; Segredo-Otero and Sanjuán, 2020; Sa Ribero et al., 2020; Voigt et al., 2016) using a Poisson probability density at a rate J (Segredo-Otero and Sanjuán, 2020) and stay immunized for a certain time (Iyer et al., 2017; Michael Lavigne et al., 2021) before becoming infectable again (called paracrine protection); once a type II site becomes infected, interference of cellular assembly and replication processes imposes a reduced rate of shed virions during the shedding phase by introducing a pre-factor $(1-\xi(u))$, where $\xi(u) = \frac{u}{u+c}$ (called autocrine protection).

Virions can also be disarmed by the action of antibodies. Antibodies (Ab) transiently bind to virion spikes, and accumulate at a prescribed rate that depends on [Ab] (Ab concentration) as well as Ab-spike binding and unbinding rates. We refer to the companion paper (Chen et al., 2022b) for details of the stochastic model for Ab protection; in our hybrid model, we choose the [Ab]-dependent accumulation rate and the saturation level of Ab-coverage of spike binding sites consistent with the stochastic model in Chen et al. (2022b). This process of Ab-coverage of viral spikes, thereby preventing spike binding to receptors on type II alveolar cells, is called *neutralization*. There are additional Ab-protection mechanisms that have been explored for other viral infections that are not explicit in the current model. One mechanism is agglutination, where Ab crosslink multiple virions, creating easier targets for immune cells. Yet another mechanism is opsonization, where Ab crosslink bound virions to Fc receptors on the surface of phagocytic cells, triggering phagocytosis whereby an immune cell engulfs and destroys the virion. Another, potentially potent Ab-protection mechanism is modeled and explored in Chen et al. (2022b), whereby Ab crosslink virions to domains on the polymeric molecules either in mucus layers of the respiratory tract or in alveolar fluid. Since the current focus of our hybrid model is not to track individual Ab or virions, nor explicitly resolve the alveolar liquid, all Ab-induced depletion effects on virions are implicitly modeled with a virion depletion term with rate $\nu w v$.

Evolution of the concentrations of infectious virions v, interferons u and antibodies w is modeled by the following PDEs in domain Ω,

$$v_t = \nabla\cdot(D\nabla v) + \chi_{\xi(\mathbf{x})=2}\ \chi_{\tau_1\le\tau\le\tau_2}\ (1-\xi(u))\lambda - dv - \kappa u v - \nu w v - \sigma v\ \chi_{\xi(\mathbf{x})=2}\ \chi_{0\le\tau\le\tau_3}, \tag{1}$$

$$0 = \nabla\cdot\left(D_u\nabla u\right) + \chi_{\xi(\mathbf{x})=2}\ \chi_{\tau_1\le\tau\le\tau_2}\ \lambda_u, \tag{2}$$

$$0 = \nabla\cdot\left(D_w\nabla w\right) - \mu v f(w), \tag{3}$$

equipped with appropriate boundary conditions on $\partial\Omega$ and initial conditions on all species concentrations. Here D, D_u, D_w are the diffusivities of virions, interferons (IFN) and antibodies (Ab), respectively, in the alveolar fluid taken constant for simplicity. All rates, $d, \lambda, \lambda_u, \mu, \nu, \sigma, \kappa, d$, are described in Table 2. In Eqs. (2) and (3) we set the derivatives $u_t = 0$, $w_t = 0$ due to the fact that interferon and antibody molecules diffuse far more rapidly than virions, thereby imposing and updating a quasi-steady state of interferons and Ab. The $f(w)$ term is an Ab depletion function that could be linear, e.g., just w, or a more complicated nonlinear form given justification. The parameter μ is nonzero when Ab experience a depletion relative to the quasi-steady concentration levels. This scenario is to accommodate outlier scenarios, such as immuno-compromised individuals with sufficiently low [Ab] that Ab-binding to viruses would cause a measurable depletion.

We simulate the cell dynamics of type II cells as an interacting particle system (Liggett, 1985), which is a continuous time Markov process, with transition rates dictated by virion and interferon concentrations at a cell site, $\Phi(\mathbf{x},t;v)$, $\Psi(\mathbf{x},t;u)$. We typically use a monod function for $\Phi(\mathbf{x},t;v) := \frac{v(\mathbf{x},t)}{v(\mathbf{x},t)+\theta_v}$ and $\Psi(\mathbf{x},t;u) := \frac{u(\mathbf{x},t)}{u(\mathbf{x},t)+\theta_u}$, rather than a linear function with a cutoff (such that above $v=\theta_v$ or $u=\theta_u$, the transition rates hit a maximum of 1), since biological processes are seldom purely linear. For the monod choice, the parameter $\theta_v \ge 0$ is the virion half-saturation concentration and $\theta_u \ge 0$ is the IFN half-saturation concentration.

A healthy type II cell occupying site $\mathbf{x}$ becomes infected at rate $\beta\Phi(\mathbf{x},t;v)$ if $\Phi(\mathbf{x},t) > 0$, and an infected type II cell is killed by immune cells at rate $-\delta\Psi(\mathbf{x},t;u)$ if $\Psi(\mathbf{x},t) > 0$. The parameters β and δ are key model parameters, the former chosen consistent with alveolar infection results in Chen et al. (2022a); the latter tunes the degree of immune response by macrophages or natural killer cells. In our model we incorporate the option of a dead type II cell to be replaced by mitosis with probability p_r, by differentiation of nearby living type I cells.

3. Implementation

The domain Ω is a square lattice containing $N\times N$ equally spaced lattice nodes. The width of a cell, h μm, dictates the two-dimensional lattice spacing so the total surface area of Ω is $Nh\times Nh$.

We define $V^n_{i,j}$ $U^n_{i,j}$, $W^n_{i,j}$ to be the numerical approximations of $v(\mathbf{x}_{i,j},t_n)$, $u(\mathbf{x}_{i,j},t_n)$, $w(\mathbf{x}_{i,j},t_n)$, respectively, where $\mathbf{x}_{i,j}=(x_i,y_j)$ is the grid node at time $t_n = n\Delta t$. For the numerical solution of the system (1)–(3) we use for simplicity the finite difference method. At each time step, we first solve the quasi-steady Eqs. (2), (3). In Eq. (3) we use the value of V^{n-1} on the previous time step, i.e., at $t = t_{n-1}$. This allows us to decouple the equations and solve them sequentially. Observe that Eq. (2) is linear and does not depend explicitly on the other variables (i.e., V or W), but depends on the cell states, which change every time step. For the solution of the linear system resulting from the finite difference discretization of Eq. (2) we use a sparse banded solver by utilizing routines found in Davis (2006). For the potentially nonlinear equation (3) we use "artificial time stepping" by employing a type of fixed point iteration known as "pseudo-transient continuation/gradient flow" (Liu and Atluri, 2008).

Algorithm 1 Model for SARS-CoV-2 Infection in the Alveolar Space

Create a finite square lattice T_h of Ω in $\mathbb{Z}^2$, with $\Delta x = \Delta y = h$;
Let Type I (empty sites) and type II (occupied sites) cells;
Impose the initial virion state, $V_{i,j}^0 = v_0$;
Calculate time scale ratio, $ratio = \Delta t_s/\Delta t$;
Define the stochastic update counter, stoch cnt = 0;
Define the time state update, $T(\mathbf{x}) = m = 0$, for each node $\mathbf{x}$ of T_h;
for $n = 1, \cdots, n_{max}$ **do**
  if $(n-1) =$ stoch cnt $\times\, ratio$ **then**
    stoch cnt + +;
    for cell, $c_{\mathbf{x}}$, $T(\mathbf{x}) = m$, from list of dead cells, C_d **do**
      Randomly choose a value, s, in $[0, 1]$;
      if $s \le p_r$ **then**
        Replace $c_{\mathbf{x}}$, $\xi(\mathbf{x}) \leftarrow 1$;
      end if
      $T(\mathbf{x}) = m + 1$;
    end for
    for cell, $c_{\mathbf{x}}$, $T(\mathbf{x}) = m$, from list of live type II cells, C_l **do**
      if $c_{\mathbf{x}}$ is an immunized cell **then**
        $t_{immun} = t_{immun} + \Delta t_s$;
        if $t_{immun} \ge \tau_4$ hours **then**
          make the cell infectable again;
        end if
      else if $\xi(\mathbf{x}) = 2$ **then**
        if $\tau \ge \tau_2$ hours **then**
          Cell, $c_{\mathbf{x}}$, killed, is removed from, C_l and $\xi(\mathbf{x}) \leftarrow -1$;
        end if
        if $\tau < \tau_2$ hours **then**
          Calculate, $\Psi(\mathbf{x}, t_n, U_{i,j}^n)$;
          if $\Psi(\mathbf{x}, t_n; V) > 0$ **then**
            Randomly choose a value, s, in $[0, 1]$;
            if $s \le \delta\Psi(\mathbf{x}, t_n)\Delta t_s$ **then**
              Cell, $c_{\mathbf{x}}$, killed, is removed from, C_l and $\xi(\mathbf{x}) \leftarrow -1$;
            end if
            $\tau = \tau + \Delta t_s$
          end if
        end if
      else if $\xi(\mathbf{x}) = 1$ **then**
        Randomly choose a value, s, in $[0, 1]$;
        if $s < p_{immunization}$ **then**
          immunize the cell, $c_{\mathbf{x}}$, and set, t_{immun}, to zero;
        else if $s < \beta\Phi(\mathbf{x}, t_n)\Delta t_s$ **then**
          Infect $c_{\mathbf{x}}$, $\xi(\mathbf{x}) \leftarrow 2$;
          $\tau = 0$
        end if
      end if
      $T(\mathbf{x}) = m + 1$;
    end for
  end if
  Update time $t_n = n\Delta t$;
  Update $V_{i,j}^n, U_{i,j}^n, W_{i,j}^n$ using numerical schemes for solving (1)-(3);
end for

For the virion equation (1) we use a fully discrete, implicit explicit numerical scheme, treating the Laplacian term explicitly and using for simplicity a second-order finite difference scheme for spatial discretization. The linear uptake or sink terms containing V^n are treated implicitly for improved stability. Observe that in every time step, we first solve the IFN and Ab equations, thus we have the U^n, W^n needed to find V^n. Our scheme solves Eqs. (1) and (3) componentwise without assembling a matrix; for Eq. (2) we efficiently store the matrix factorization from the beginning ($t = 0$) and apply it to solve the corresponding linear system in subsequent time steps. For our tests, von Neumann or matrix stability analysis dictates we take the following stable time step:

$$\Delta t < \frac{h^2}{4D}. \tag{4}$$

In order to simulate the continuous time Markov chain model for the lattice cell site dynamics, we simulate its embedded discrete time process. We do that by updating all states occupied by healthy type II cells sites at every "stochastic" time step Δt_s, which is possibly (much) larger than Δt. The transition probabilities for a type II cell to be infected (provided $\Phi(\mathbf{x}, t; v) > 0$) are given by $P(\text{infection}) = \beta\Phi(\mathbf{x}, t; v)\Delta t_s$; similarly the transition probability of an infected type II cell to be killed by immune cells (provided $\Psi(\mathbf{x}, t; u) > 0$ and $\tau < \tau_2$) is $P(\text{killing}) = \delta\Psi(\mathbf{x}, t; u)\Delta t_s$.

In the implementation we update the state of each site only once within a stochastic time step. We also want the number of "transition events" (i.e. infections or deaths) within each stochastic update to be relatively small to align with the behavior of the continuous time process model. By assigning a flag to each grid node, we track whether a selected lattice site has already been updated within the same stochastic time step. By choosing Δt_s, β and δ appropriately we maintain a low number of transition events per stochastic update cycle. In the algorithm, for efficiency, we update the state of lattice sites by only cycling through live type II cells.

An important issue in the implementation scheme is the coupling of the stochastic cell model and the continuous PDEs. Namely, we simulate the stochastic cell model by using its embedded discrete time process. Since the continuum dynamics evolves in time according to a discrete time step Δt, we advance the cell dynamics model in the same way by performing synchronous updating of the state at each lattice site at every prescribed stochastic time step Δt_s. The implementation of the entire procedure is described in detail in algorithm 1, and we implemented it using the C-programming language, creating flexible data structures. The algorithm is partially based on work done in Aristotelous and Durrett (2014b,a), and is inspired by Richardson (1973).

Table 1
Base parameter values.

Base parameters	Values
D	1.27 μm^2 s^{-1} Lai et al. (2009)
D_u	95 μm^2 s^{-1} Kreuz and Levy (1965)
D_w	40 μm^2 s^{-1} Olmsted et al. (2001) and Saltzman et al. (1994)
λ	1 K virions day^{-1}cell^{-1} Bar-On et al. (2020)
λ_u	0.6 [#IFN units] [mm^2]$^{-1}$ [h]$^{-1}$cell^{-1} Segredo-Otero and Sanjuán (2020)
τ_1	12 h Bar-On et al. (2020)
τ_2	84 h Park et al. (2021)
τ_3	24 h Cummings et al. (2012)
d	2.27% min^{-1} Smither et al. (2020)
β	0.06 cell^{-1} s^{-1} Chen et al. (2022a)
θ_v	5 [#of virions] (μm^2)$^{-1}$

4. Simulation results

4.1. Model variables and parameters

Simulations require choices for many parameters 2. Base parameters listed in Table 1 were taken from the published literature. Other model parameters are chosen based on logical biological assumptions; for others, we vary the parameters to explore sensitivity in viral load and infected cells in our model, and thereby learn values that tune the model to certain outcomes.

For the infection probability function $\Phi(v)$ we choose the parameter θ_v such that $\Phi(v) \approx 1$ when the 2D type II cell (4 μm×4 μm) is saturated by virions (1600 virions are needed to completely cover (saturate) a 2D "square" cell). In the absence of single cell data, this choice is consistent with predictions of the stochastic model. For our simulation

Table 2
Variable and parameter descriptions.

Variables	Descriptions	Units
v	Virion concentration	[# of virions] [area]$^{-1}$
u	IFN concentration	[# of IFN units] [area]$^{-1}$
w	Ab concentration	[mass] [area]$^{-1}$
Base parameters		
D	Virion diffusivity	[area]^2 [time]$^{-1}$
D_u	IFN diffusivity	[area]^2 [time]$^{-1}$
D_w	Ab diffusivity	[area]^2 [time]$^{-1}$
λ	Virion shedding rate	[# virions] [cell]$^{-1}$ [time]$^{-1}$ [area]$^{-1}$
λ_u	IFN release rate	[# IFN units] [cell]$^{-1}$ [time]$^{-1}$ [area]$^{-1}$
τ_1	Duration of eclipse phase	[time]
τ_2	Duration of cell infection phase	[time]
τ_3	Duration of cell virion-uptake phase	[time]
d	Virion decay rate	[time]$^{-1}$
β	Virion-induced healthy-to-infected cell switching rate	[time]$^{-1}$ cell^{-1}
θ_v	Virion half-saturation concentration	[v]
Modeling parameters		
δ	IFN-induced infected-to-dead cell switching rate	[time]$^{-1}$ cell^{-1}
θ_u	IFN half-saturation concentration	[u]
u_c	IFN-level tuning of reduced cell replication rate	[u]
κ	IFN-induced virion depletion rate	[u]$^{-1}$ [time]$^{-1}$
σ	Virion reabsorption rate of infected cells	[cell]$^{-1}$ [time]$^{-1}$
ν	Ab-induced virion depletion rate	[w]$^{-1}$ [time]$^{-1}$
μ	Virion-induced Ab depletion rate	[u]$^{-1}$ [time]$^{-1}$
τ_4	Duration of cell refractory phase	[time]
J	Immunization rate per cell	[cell]$^{-1}$ [time]$^{-1}$ [# IFN units]$^{-1}$ [area]

tests, we set the eclipse phase duration to $\tau_1 = 12$ h starting at the time of infection, and set the "shedding" phase duration that begins immediately after eclipse to 72 h, thus $\tau_2 = 84$ h. For all simulations we use a 500×500 interior node grid with spacing $dx = 4$ μm, hence a type II cell is considered to be "square" with area 16 μm^2. Type II cells occupy approximately 30% of the grid nodes.

4.2. Pre-immunity

To begin, we illustrate the baseline, pre-immunity, results of our model by decoupling the equations for Ab (3) and IFN (2), hence no immune response is present. We also set $\sigma = 0$ in Eq. (1), i.e., turning off the virion reabsorption rate of infected cells. We then impose a single infected type II cell positioned in the middle of the computational domain that has just been infected and therefore is starting the eclipse phase. The infection then progresses according to our algorithm 1. The simulation results, for the stated choice of input parameters, are shown in Fig. 1, showing snapshot profiles of the infected cells and virions during their evolution.

We observe that the infection spreads gradually in a symmetric manner reaching the artificial finite boundary where virions are absorbed. The transition of infected cell states from eclipse to shedding and then death follows the deterministic rules of our algorithm. In subsequent simulations, the presence of interferon-induced immune responses (lower probability to become infected, lower replication and shedding rate of progeny) will interfere with these results, to degrees tuned by the degrees and types of response.

Next we concentrate on the possibility that once infected, type II cells continue to allow virion binding to receptors and cell uptake. This virion sink from infected cell sites has a duration time, τ_3; we use the literature estimate of 24 h (Cummings et al., 2012). To investigate this effect, we perform tests by varying the virion-uptake parameter σ of infected cells in Eq. (1). Results are given in Fig. 2.

We observe that larger rates of absorption of virions by infected cells, i.e., larger σ, result in fewer infected cells and shed virions, not surprisingly. Whether and the degree to which this phenomenon is associated with SARS-CoV-2 alveolar infection is to be determined by dedicated experiments. Some level of continued virion absorption by infected cells is highly likely, so *for the remainder of this paper we fix* $\sigma = 1$ h^{-1} cell^{-1}. We also compared the infection radius, the infected cell numbers and virion count at $t \approx 48$ h, with results generated by the stochastic model used in Chen et al. (2022a) and in Chen et al. (2022b), and find reasonable agreement with this degree of continued binding and uptake of virions by alveolar type II cells.

4.3. Innate immune responses

Using the base parameters and values given in Table 2, we now turn on immune response mechanisms triggered by IFNs, first individually and then collectively. To do so, we couple the IFN Eq. (2) while continuing to suppress Ab protection with Eq. (3) turned off. We defer the model predictions of coupled IFN and Ab protection to future studies. The model has four distinct IFN concentration-dependent mechanisms: (i) once a type II cell is infected, interference of the cellular processes of assembly, replication, and shedding of infectious progeny, where the degree of interference is tuned by the factor $1 - \xi(u)$ in Eq. (1); (ii) signaling of macrophages to eliminate virions, modeled by $-\kappa v u$ in Eq. (1); (iii) signaling of macrophages or natural killer (NK) cells to terminate infected type II cells either in the eclipse or shedding phases, thus aborting the deterministic clock of infected cells, modeled by an IFN-dependent probability, $P(\text{killing}) = \delta \Psi(\mathbf{x}, t; v) \Delta t_s$, in algorithm 1; (iv) finally, the paracrine effect (Sa Ribero et al., 2020; Voigt et al., 2016), leading to total immunization of healthy type II cells for a certain time period τ_4, is simulated by including an IFN-dependent immunization probability,

$$p_{immunization}(u; J) = 1 - \exp(-\Delta t_s J u) \tag{5}$$

such that at each stochastic time step, Δt_s, healthy type II cells become immunized with probability $p_{immunization}$, and J is the immunization rate. The immunized cell becomes infectable again after τ_4 hours in algorithm 1.

4.3.1. IFN-induced disruption of virion assembly, replication and shedding by infected cells

We first isolate IFN-induced limiting of virion assembly and replication by infected cells in the eclipse phase, and therefore reduced virion shedding rate in the shedding phase. To do so, we turn on the shedding rate pre-factor $(1 - \xi(u))$ in Eq. (1), and we turn off all other IFN-induced protections. The function $\xi(u) = u/(u + u_c)$ has tuning parameter u_c, and we illustrate effects of limited replication and shedding with three choices, $u_c = 0.1,\ 0.01,\ 0.001$. Small u_c values model significant disruption; with u_c closer to 0, ξ is closer to 1, and the

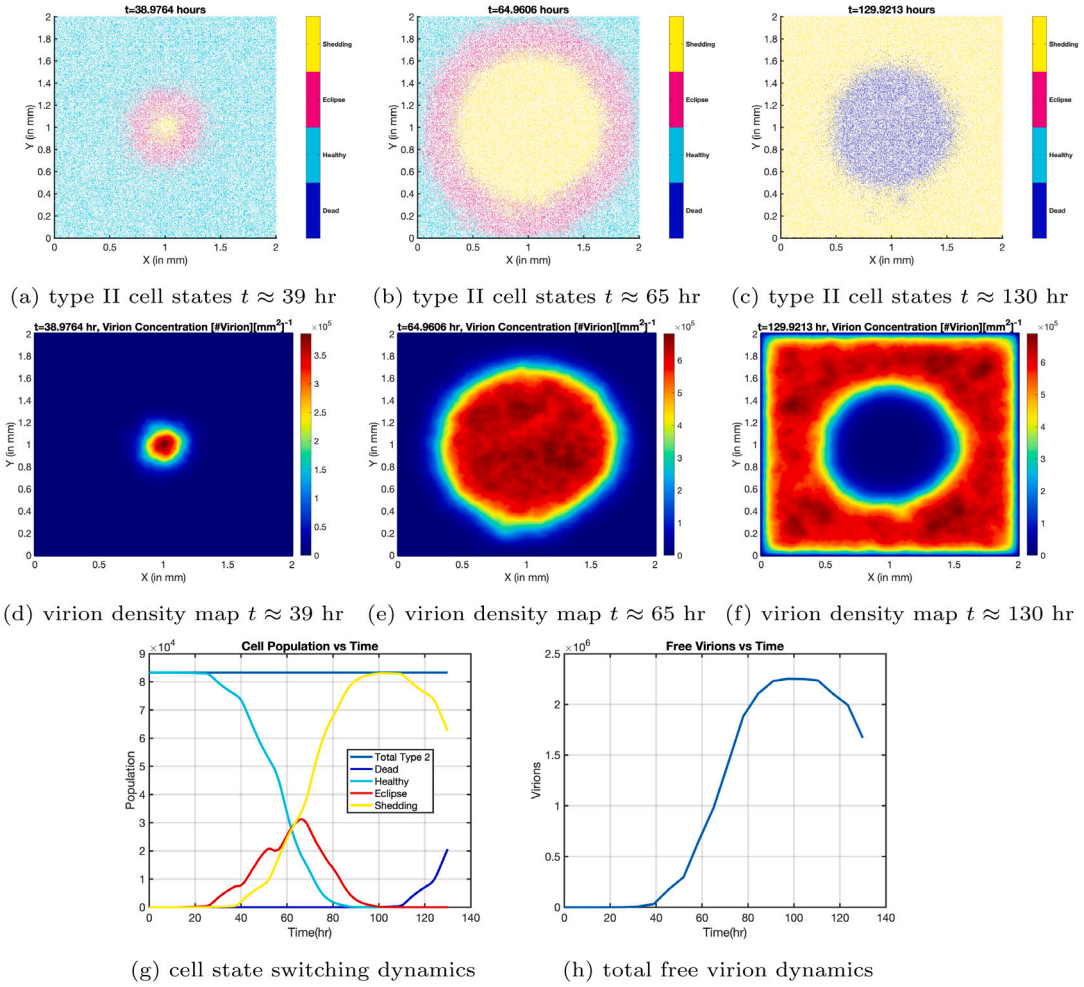

(a) type II cell states $t \approx 39$ hr (b) type II cell states $t \approx 65$ hr (c) type II cell states $t \approx 130$ hr

(d) virion density map $t \approx 39$ hr (e) virion density map $t \approx 65$ hr (f) virion density map $t \approx 130$ hr

(g) cell state switching dynamics (h) total free virion dynamics

Fig. 1. Baseline model simulation of pre-immune alveolar infection without virion absorption by infected cells, i.e., $\sigma = 0$. Row 1 shows snapshots at 39, 65, 130 h of the spread of type II cell infection starting from a centrally located single infected cell, where $t = 0$ marks onset of the eclipse phase. Cyan signifies a healthy type II cell, dark pink an infected type II cell in eclipse phase, yellow an infected type II cell in shedding phase, and dark blue a dead type II cell. Row 2 shows average virion concentration heat maps (color bars indicate local virion levels) corresponding to the infected cell snapshots in Row 1. Row 3, panel g shows the evolution throughout 130 h of healthy vs. infected cell count, as well as the counts of infected cells in the eclipse, shedding, and dead phases; Row 3, panel h shows the corresponding evolution of free virions. The reversals and plateaus near 100 h are artificial boundary effects as virions and infection reach the boundary of the computational domain.

pre-factor $(1-\xi(u))$ is closer to 0, virtually eliminating the virion source from infected cells. The limiting value $u_c = 0$ corresponds to complete disabling of replication and shedding.

Results are presented in Fig. 3, comparing snapshots of the spatial spread in the computational domain at 70 h post infection from a single type II cell of: infected cells (Row 1), shed viral load (Row 3) and IFN load (Row 5). Row 2 shows the time evolution through 140 h of the total cell distribution: healthy cells, infected cells in the eclipse phase, shedding cells, and dead cells. Row 4 shows the time evolution of free virions through 140 h. The degree of IFN-induced disruption of infected cell replication increases from left to right: u_c decreases ($u_c = 0.1$, Column 1) to ($u_c = 0.01$, Column 2) to ($u_c = 0.001$, Column 3).

Rows 1 and 3, respectively, show progressively stronger disruption of virion shedding by infected cells, with infected cells and virions both *slowing and becoming asymmetric*. Once virions reach the boundary of the computational domain, artificial effects start to creep into the results due to absorbing boundary conditions, which is why we present snapshots at $t = 70$ h where boundary effects have yet to have a measurable influence. At the strongest IFN-induced disruption setting, $u_c = 0.001$, Column 3, secondary infections are spawned correlated with isolated hot spots of high virion load, producing more heterogeneous infected cell and free virion spatial morphologies. In results not presented here, the hints of asymmetry and heterogeneity in Fig. 2 at higher virion absorption rates σ by infected cells, when coupled with strong suppression of virion replication and shedding, further amplify secondary hot spots and heterogeneity. In interacting particle system growth models like the present one, similar heterogeneous behaviors due to local sinks of a diffusing field are common and were observed in Aristotelous and Durrett (2014b).

4.3.2. *IFN-induced signaling of macrophages to eliminate virions*

In this section we turn on IFN-induced signaling of macrophages that eliminate virions via phagocytosis, and all other immune protection mechanisms are turned off. To do so, we include the nonlinear virion sink term $-\kappa uv$ in (1) that involves the product of virion and IFN concentrations. This mechanism is therefore qualitatively different from the constant source of virions by infected, shedding cells, and the IFN-induced damping of this constant source. Therefore we are compelled to explore the sensitivity of the progression of infection and viral load to this nonlinear sink mechanism, and to understand what orders of magnitude of the sink strength, κ,induce what degrees of macrophage protection when they are acting alone. This parameter-tuning exercise gives information of how the model reflects the degrees of IFN-signaled macrophage protection, from very weak to very strong.

Fig. 4 illustrates the effect of this mechanisms for $\kappa = 10,\ 50,\ 100$. Clearly, increasing κ reduces infected cell and free virion counts, but

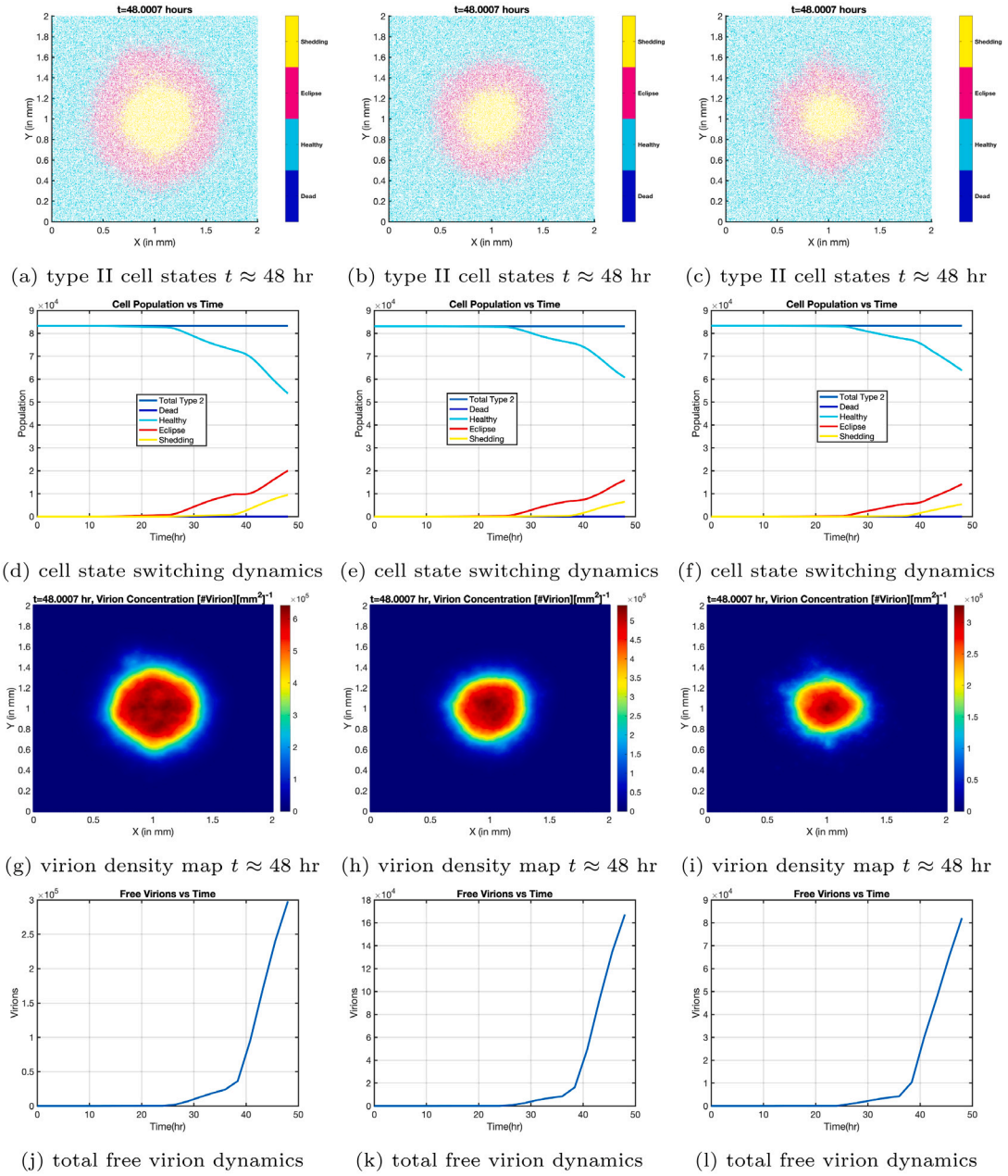

(a) type II cell states $t \approx 48$ hr (b) type II cell states $t \approx 48$ hr (c) type II cell states $t \approx 48$ hr

(d) cell state switching dynamics (e) cell state switching dynamics (f) cell state switching dynamics

(g) virion density map $t \approx 48$ hr (h) virion density map $t \approx 48$ hr (i) virion density map $t \approx 48$ hr

(j) total free virion dynamics (k) total free virion dynamics (l) total free virion dynamics

Fig. 2. Sensitivity of alveolar pre-immune infection to virion absorption rate by already infected cells. The degree of virion absorption by infected cells is tuned by the absorption rate parameter σ: $\sigma = 0$ in Column 1, $\sigma = 1$ in Column 2, and $\sigma = 5$ in Column 3. Rows 1 and 3 show, for each fixed σ, spatial lattice snapshots at $t \approx 48$ h after infection at $t = 0$ of a single type II cell. Row 1 depicts healthy type II cells (cyan), and infected type II cells in eclipse phase (dark pink), shedding phase (yellow), and dead phase (dark blue). Row 3 depicts the virion density heat map. Row 2 shows the switching dynamics over 48 h between healthy and states of infected type II cells, while Row 3 shows the dynamics of the total free virions over 48 h.

these orders of magnitude do not produce significant protection that macrophages are believed to provide, especially since IFN-signaled macrophages are believed to be the first line of immune defense to novel pathogens Janeway et al. (2001) and Sallard et al. (2020). Hence, in Fig. 5 we test $\kappa = 10^3, 10^4, 10^5$ and observe more substantial protective effects, progressively reducing the spatial spread (Rows 1 and 3) and counts (Rows 2 and 4) of infected cells and shed virions, respectively. The IFN load likewise is progressively reduced in spatial spread and concentration (Row 5). In Rows 3, 4, 5 we call attention to the orders-of-magnitude reduction in virion and IFN concentrations from left to right as κ increases over two orders-of-magnitude. Once again, in Rows 1 and 2 we observe secondary, tertiary, and more satellite hot spots of infected cells and shed virions. The protective effect of macrophage consumption of virions is most pronounced with $\kappa = 10^5$, Column 3: after three and a half days the progression of infection is strongly arrested, and less then 50 virions remain. It would be valuable to have experimental data from alveolar cell cultures with infectious SARS-CoV-2 virions and macrophages present to compare with this experimental data and see if it is possible to learn κ.

4.3.3. IFN-induced signaling of macrophages and natural killer (NK) cells to eliminate infected type II cells

Now we proceed to explore the effect of IFN-induced phagocytosis and other cytotoxic factors of infected type II cells by macrophages and NK cells. We turn off the two IFN-induced mechanisms explored above that act in the continuum PDEs. Now, the IFN-induced signaling of macrophages and NK cells acts in the stochastic switching dynamics of the cell lattice through the killing rate parameter δ in the killing

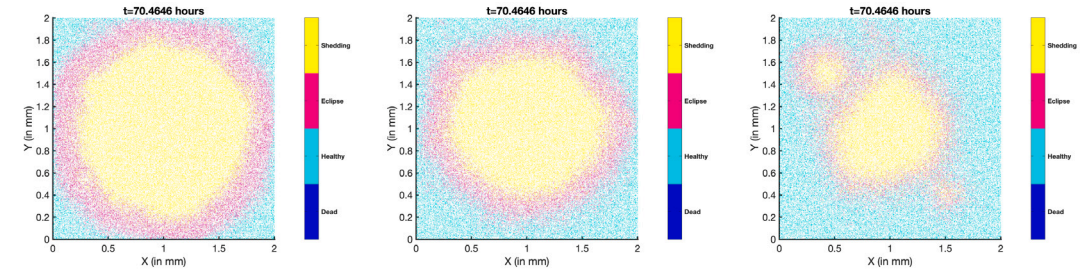

(a) type II cell states $t \approx 70$ hr (b) type II cell states $t \approx 70$ hr (c) type II cell states $t \approx 70$ hr

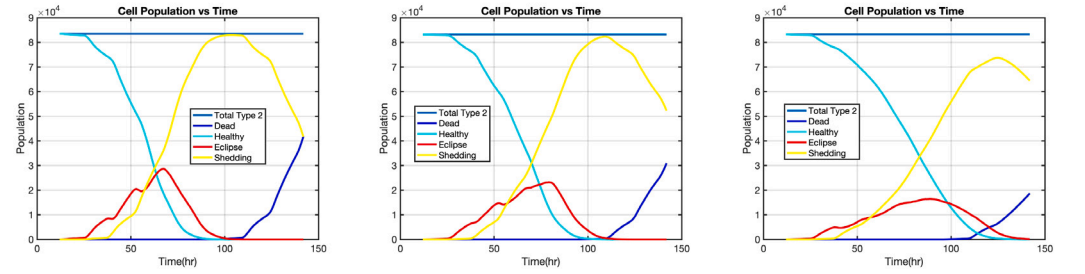

(d) cell state switching dynamics (e) cell state switching dynamics (f) cell state switching dynamics

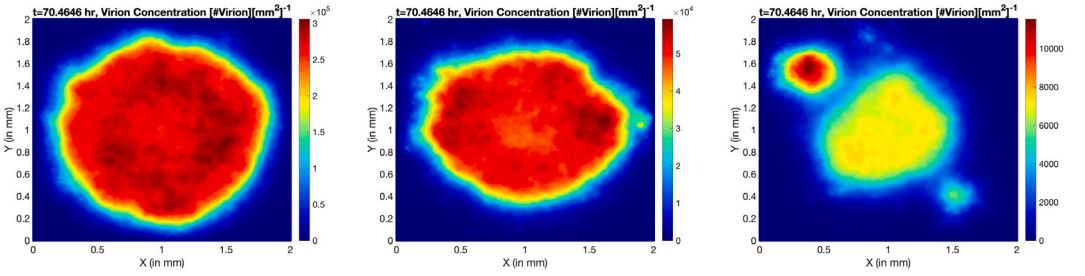

(g) virion density map $t \approx 70$ hr (h) virion density map $t \approx 70$ hr (i) virion density map $t \approx 70$ hr

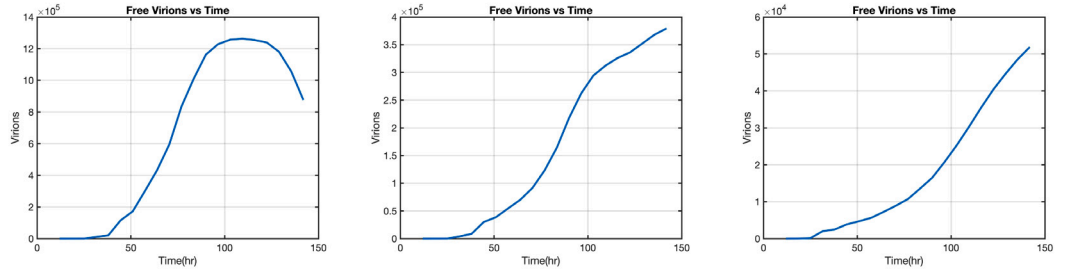

(j) total free virion dynamics (k) total free virion dynamics (l) total free virion dynamics

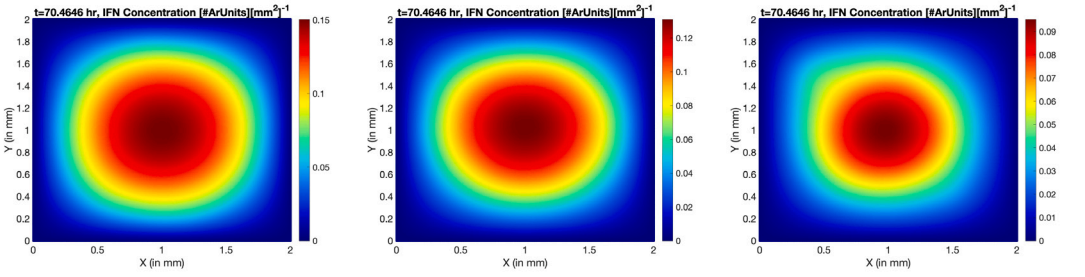

(m) IFN density map $t \approx 70$ hr (n) IFN density map $t \approx 70$ hr (o) IFN density map $t \approx 70$ hr

Fig. 3. Effects of IFN-induced suppression of virion replication and shedding by infected cells. The degree of suppression of infected cell replication and shedding of progeny is tuned by the parameter u_c: $u_c = 0.1$ in Column 1, $u_c = 0.01$ in Column 2, $u_c = 0.001$ in Column 3. Rows 1, 3, 5 show, for each fixed u_c, snapshots at $t \approx 70$ h over the spatial cell lattice of: the infected and healthy type II cells (Row 1), virion concentration heatmap (Row 3), and IFN concentration heatmap (Row 5), where $t = 0$ is the onset of infection and eclipse phase of a centrally located single infected cell. In Row 1, cyan signifies a healthy type II cell, dark pink an infected type II cell in eclipse phase, yellow an infected type II cell in shedding phase, dark blue a dead cell. Row 2 shows the infected cell population over time for each choice of u_c, and Row 3 shows the virion concentration time snapshots corresponding to the cell profiles in Row 1. Row 4 shows average virion count in the domain over time.

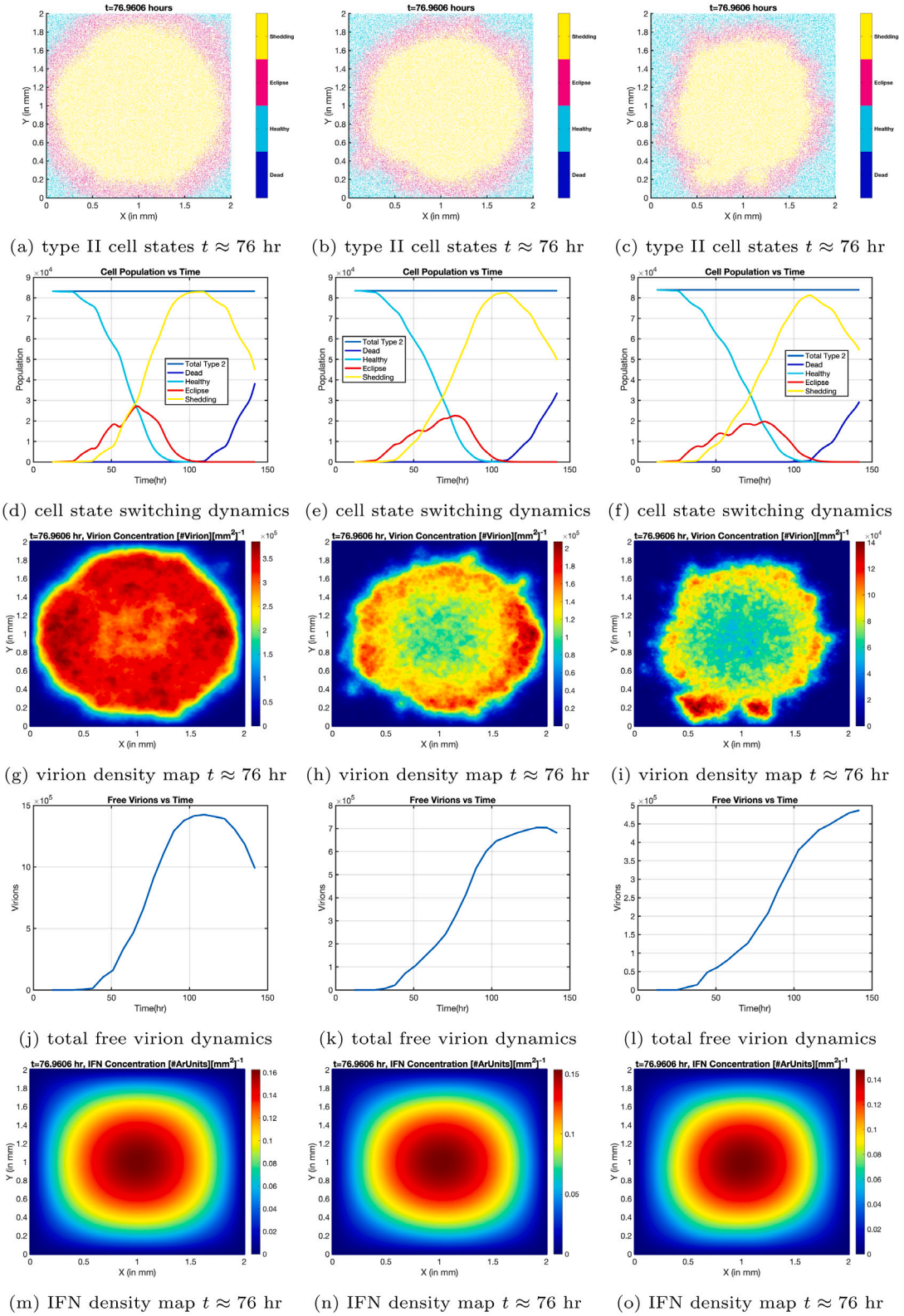

(a) type II cell states $t \approx 76$ hr (b) type II cell states $t \approx 76$ hr (c) type II cell states $t \approx 76$ hr

(d) cell state switching dynamics (e) cell state switching dynamics (f) cell state switching dynamics

(g) virion density map $t \approx 76$ hr (h) virion density map $t \approx 76$ hr (i) virion density map $t \approx 76$ hr

(j) total free virion dynamics (k) total free virion dynamics (l) total free virion dynamics

(m) IFN density map $t \approx 76$ hr (n) IFN density map $t \approx 76$ hr (o) IFN density map $t \approx 76$ hr

Fig. 4. Effects of IFN-induced signaling of macrophages to eliminate virions with *low* virion sink strengths κ. Column 1 is with $\kappa = 10$, Column is with $\kappa = 50$, Column 3 is with $\kappa = 100$. Similarly to Fig. 3, Row 1 shows the spatial spread of healthy vs. infected phases of type II cells, Row 3 shows the virion concentration heatmap, Row 5 shows the IFN concentration heatmap, where each spatial morphology is a snapshot at $t \approx 76$ h starting from one infected cell at $t = 0$ of the progression of infected type II cells. Row 2 shows the dynamic progression over time of the type II lattice site distribution across healthy and infected cells in eclipse, shedding, or death phases, and Row 4 shows the dynamic progression of virion concentration.

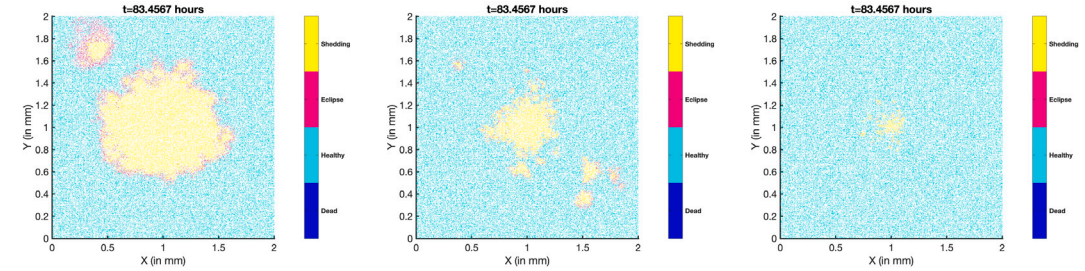

(a) type II cell states $t \approx 83$ hr (b) type II cell states $t \approx 83$ hr (c) type II cell states $t \approx 83$ hr

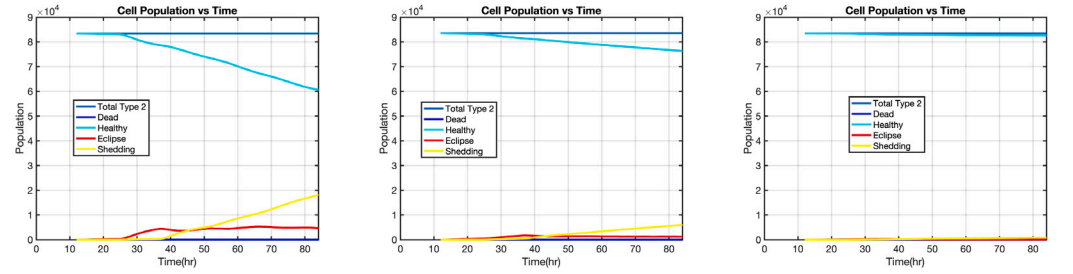

(d) cell state switching dynamics (e) cell state switching dynamics (f) cell state switching dynamics

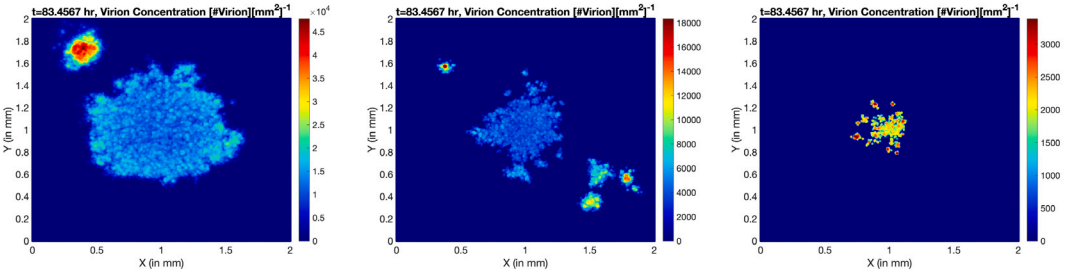

(g) virion density map $t \approx 83$ hr (h) virion density map $t \approx 83$ hr (i) virion density map $t \approx 83$

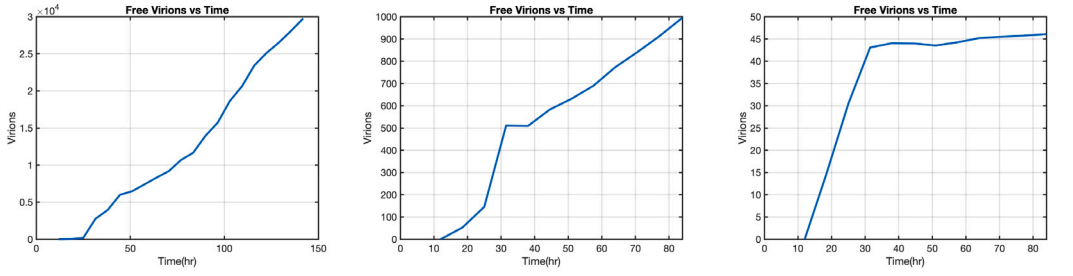

(j) total free virion dynamics (k) total free virion dynamics (l) total free virion dynamics

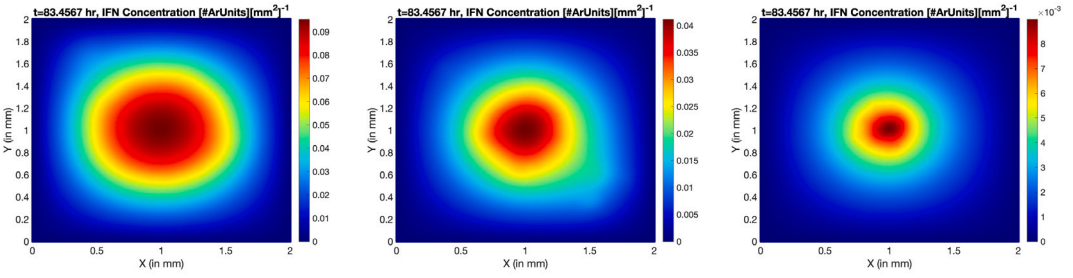

(m) IFN density map $t \approx 83$ hr (n) IFN density map $t \approx 83$ hr (o) IFN density map $t \approx 83$ hr

Fig. 5. Effects of IFN-induced signaling of macrophages to eliminate virions with *high (and significant)* virion sink strengths κ. Column 1 is with $\kappa = 10^3$, Column 2 is with $\kappa = 10^4$, Column 3 is with $\kappa = 10^5$. Similarly to Fig. 3, Row 1 shows the spatial spread of healthy vs. infected phases of type II cells, Row 3 shows the virion concentration heatmap, Row 5 shows the IFN concentration heatmap, where each spatial morphology is a snapshot at $t \approx 76$ h starting from one infected cell at $t = 0$ of the progression of infected type II cells. Row 2 shows the dynamic progression over time of the type II lattice site distribution across healthy and infected cells in eclipse, shedding, or death phases, and Row 4 shows the dynamic progression of virion concentration.

probability, $P(\text{killing}) = \delta\Psi(\mathbf{x}, t; u)\Delta t_s$. We isolate δ as the tuning parameter of this IFN mechanism by fixing $\theta_u = 0.01$ and thereby the function $\Psi(u)$. Once again we explore ranges of δ to learn how to tune weak versus strong protection degrees of protection and the impact this mechanism is capable of providing, by itself. In Fig. 6 we present results for $\delta = 0.01,\ 1,\ 50$ drawn from simulations out to $t = 84$ h post onset of infection of a single type II cell. Recall that this time is how long infected cells live in eclipse plus shedding phases before dying, so that during the simulations all dead type 2 cells have been killed by macrophages and NK immune cells.

The results reveal insights into the remarkable protection from IFN-signaling of macrophages and NK cells to eliminate infected type II cells. At the lowest strength, $\delta = 0.01$ in Column 1, the $t = 57$ h snapshots reveal early evidence of cell death (dark blue speckles in Row 1, panel a), correlated with depletion of shed virions (Row 3, panel g), with both effects correlated with the central hotspot of high IFN concentration. The stochasticity of cell death further introduces asymmetry in cell infection and viral load heatmaps. At the middle strength, $\delta = 1$ in Column 2, the $t = 57$ h snapshots reveal a higher density of cell death (Row 1, panel b), significantly higher and heterogeneous depletion of shed virions (Row 3, panel h), and the first evidence of heterogeneity in the IFN heatmap (Row 5, panel n). The stochastic switching dynamics of type II cell states and phases are revealed in Row 2, and comparison of panels d and e reveal a significant reduction of type II cells in the shedding phase, thus explaining the lower IFN heatmap levels. At the highest strength, $\delta = 50$ in Column 3, the impact of IFN-signaling of macrophages and NK cells is dramatic: the infected cell count and spread, free virion count and spread, and IFN heatmap, are heavily reduced with highly irregular spatial morphology.

4.3.4. Combined IFN-induced signaling mechanisms of immunity: suppressed virion replication and shedding by infected cells, virion depletion by macrophages, and infected cell depletion by macrophages and natural killer cells

Thus far, we have illustrated model predictions of three individual IFN-induced protection mechanisms. We now illustrate model predictions with all mechanisms turned on, compared against results from each mechanism acting by itself, to see evidence of feedback between the three mechanisms. We choose to illustrate feedback between: strong suppression of infected cell assembly, replication, and shedding of virions by setting $u_c = 0.001$; a weak IFN-signaling of macrophages and virion depletion rate by setting $\kappa = 1$; and a moderate IFN-signaling of macrophages and NK cells to kill infected cells by setting the infected cell death rate $\delta = 1$. Fig. 7 compares the outcomes at ≈ 57 h post cell infection of: type II cell states, Column 1, virion density heatmap, Column 2, and IFN density heatmap, Column 3. Results for the combined protective mechanisms are in Row 1, protection only from the moderate death rate $\delta = 1$ of infected cells by macrophages and NK cells is in Row (2), protection only from the weak virion depletion rate $\kappa = 1$ of virions by macrophages is in Row 3, and protection only from strong suppression of infected cell shedding rate of virions with $u_c = 0.001$ is in Row 4.

We note here that any "dead" cell observed in our simulations is a previously infected type II cell killed by immune cells, so we consider dead cells in this section as part of the infection profile. In Fig. 7, we can see that the combined simulation in the first row, has a reduced infected/dead cell region size and reduced virion count, in comparison with the simulation in the second row — which has only the killing of infected type II cells mechanism turned on.

We may be tempted to conclude that the result is as expected, but there is more to the story, since if we observe the infected cell profiles in rows 3 and 4 we can see that they are comparable in size or smaller than the combined simulation profile. This is counter-intuitive, because a cumulative effect of immune responses (including all the parameters combined as in each case depicted in rows 2–4) is expected to produce a significantly smaller cell infection profile than all the profiles corresponding to the individual IFN-induced mechanisms tests.

The reason for this discrepancy is the different IFN concentrations between each test, for example between rows 1 and 3. The IFN concentration in row 3 is higher than the one in the combined test depicted in row 1, so the IFN positive feedback mechanism, observed in row 3 to promote increased virion killing, is comparatively under-performing in row 1 because the IFN concentration is more than one order of magnitude lower. This allows the virions in row 1 to spread outside the main infection region, without being killed at the same aggressive rate as in the scenario described in row 3.

We note that all IFN-induced immune mechanisms depend explicitly on the IFN concentration u. Thus, a combination of these three mechanisms could result in smaller u concentrations for example due to killing of shedding type II cells which in our setup are the only ones producing IFNs, and thus lowering the IFN concentration in the infected region, therefore negatively impacting the intensity of an individual IFN immune response in comparison with the case when this mechanism is the only one turned on.

So an infection like the one described in row 1 would eventually slowly infect all the healthy cells, due to the nature of the dependence of the immunity mechanisms on the reduced IFN levels, in our setup.

The model illuminates an issue–the need for a separate mechanism that can sustain the IFN concentration at high enough levels to completely kill the infection. At the same time, maintaining this high IFN concentration is challenging, since elimination of infected type II cells and slowing rates of infection result in fewer infected IFN-producing cells. This paradoxical effect may explain why immune cells evolved to also produce IFN, e.g., IFN I and II (Lee and Ashkar, 2018; Liu et al., 2012) which do exactly that, i.e., maintain a high IFN concentration even after infected cells are killed.

IFN produced by immune cells can thus help a healthy immune system better fight a viral infection, possibly preventing the infection from slowly persisting and spreading through the entire tissue.

To our knowledge, many published models model IFN production only from infected cells, for example Segredo-Otero and Sanjuán (2020) and Moses et al. (2021), which is consistent with type I IFN (Mantlo et al., 2020) and other IFN produced by infected cells only. We plan in the next iteration of our model to account for IFN generated by immune cells, in order to make our framework more biologically accurate.

4.3.5. IFN-induced paracrine effect on infectable cells.

In this section we examine the effect of the fourth IFN-induced mechanism, which immunizes infectable cells according to IFN concentration, u. Paracrine signaling of IFN turns neighboring infectable cells to cells refractory to infection (Sa Ribero et al., 2020; Voigt et al., 2016). We model this at each stochastic time step, Δt_s, by immunizing healthy infectable cells with Poisson probability density defined previously in Eq. (5). A cell remains immunized for a certain time interval, which published literature suggested to be $\tau_4 = 24$ h (Michael Lavigne et al., 2021; Iyer et al., 2017), before it becomes infectable again (see algorithm 1). Here the immunization rate value from published literature (Segredo-Otero and Sanjuán, 2020) is taken to be $J = 0.01$ cell^{-1} min^{-1} [# IFN units]$^{-1}$ cm^2. In Fig. 8 we see that the paracrine effect is a powerful mechanism capable of significantly slowing the spread of the infection with the specific choice of parameter values. In Fig. 8-column 1 we plot the base case (without the paracrine effect), containing the combined effect of the first three IFN-induced mechanisms studied before, and shown for a shorter time interval in Fig. 7-row 1. We compare this with the simulations in Fig. 8-columns 2 and 3, depicting the effects of the paracrine protection mechanism. Specifically Fig. 8-column 2 shows what happens if only the paracrine effect is turned on. We can see from panel 8(b) that only the paracrine effect is capable, even after 142 h, to keep the infected area contained in a disk of diameter ≈ 1, in contrast with the case where all IFN-induced mechanisms but the paracrine effect

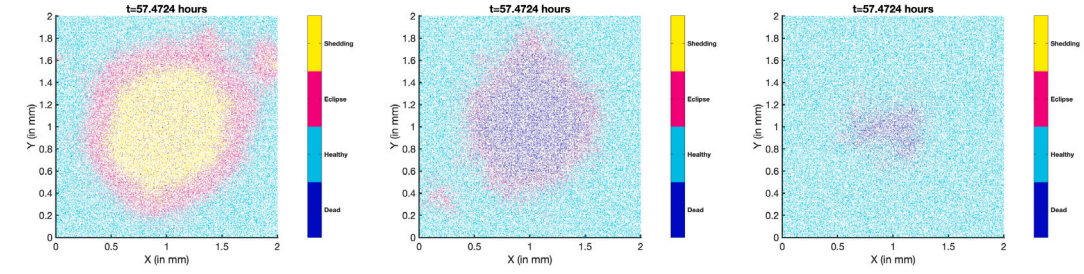

(a) type II cell states $t \approx 57$ hr (b) type II cell states $t \approx 57$ hr (c) type II cell states $t \approx 57$ hr

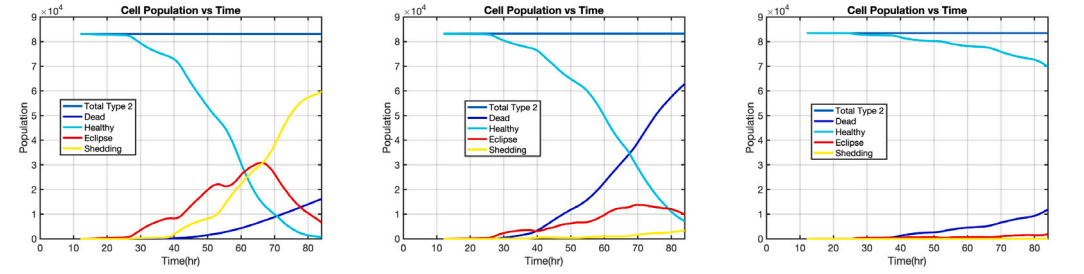

(d) cell state switching dynamics (e) cell state switching dynamics (f) cell state switching dynamics

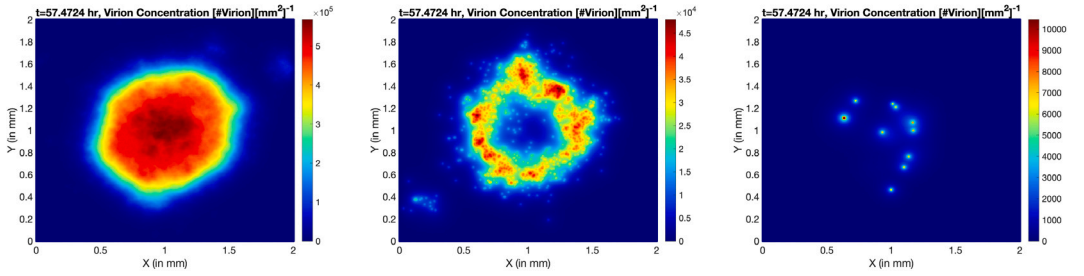

(g) virion density map $t \approx 57$ hr (h) virion density map $t \approx 57$ hr (i) virion density map $t \approx 57$ hr

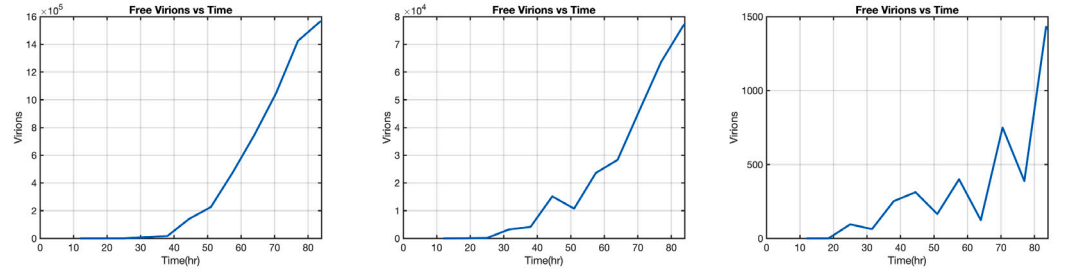

(j) total free virion dynamics (k) total free virion dynamics (l) total free virion dynamics

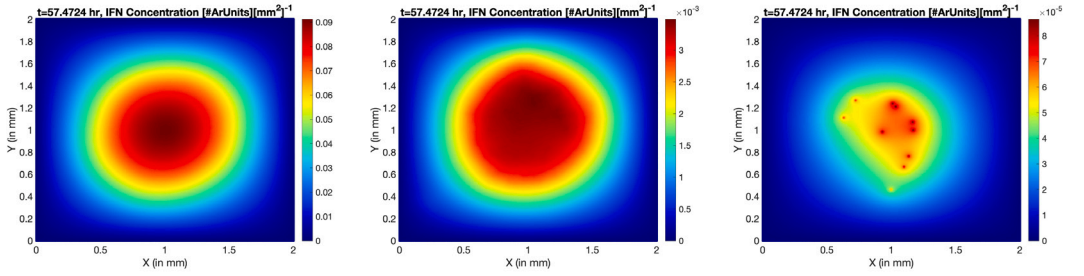

(m) IFN density map $t \approx 57$ hr (n) IFN density map $t \approx 57$ hr (o) IFN density map $t \approx 57$ hr

Fig. 6. Effects of IFN-induced signaling of macrophages and NK cells to kill infected type II cells with killing rate parameter δ. Column 1 is with $\delta = .01$, Column 2 is with $\delta = 1$, Column 3 is with $\delta = 50$. Row 1 shows the spatial spread of healthy vs. infected phases of type II cells, Row 3 shows the virion concentration heatmap, Row 5 shows the IFN concentration heatmap, where each spatial morphology is a snapshot at $t \approx 76$ h starting from one infected cell at $t = 0$ of the progression of infected type II cells. Row 2 shows the dynamic progression over time of the type II lattice site distribution across healthy and infected cells in eclipse, shedding, or death phases, and Row 4 shows the dynamic progression of virion concentration.

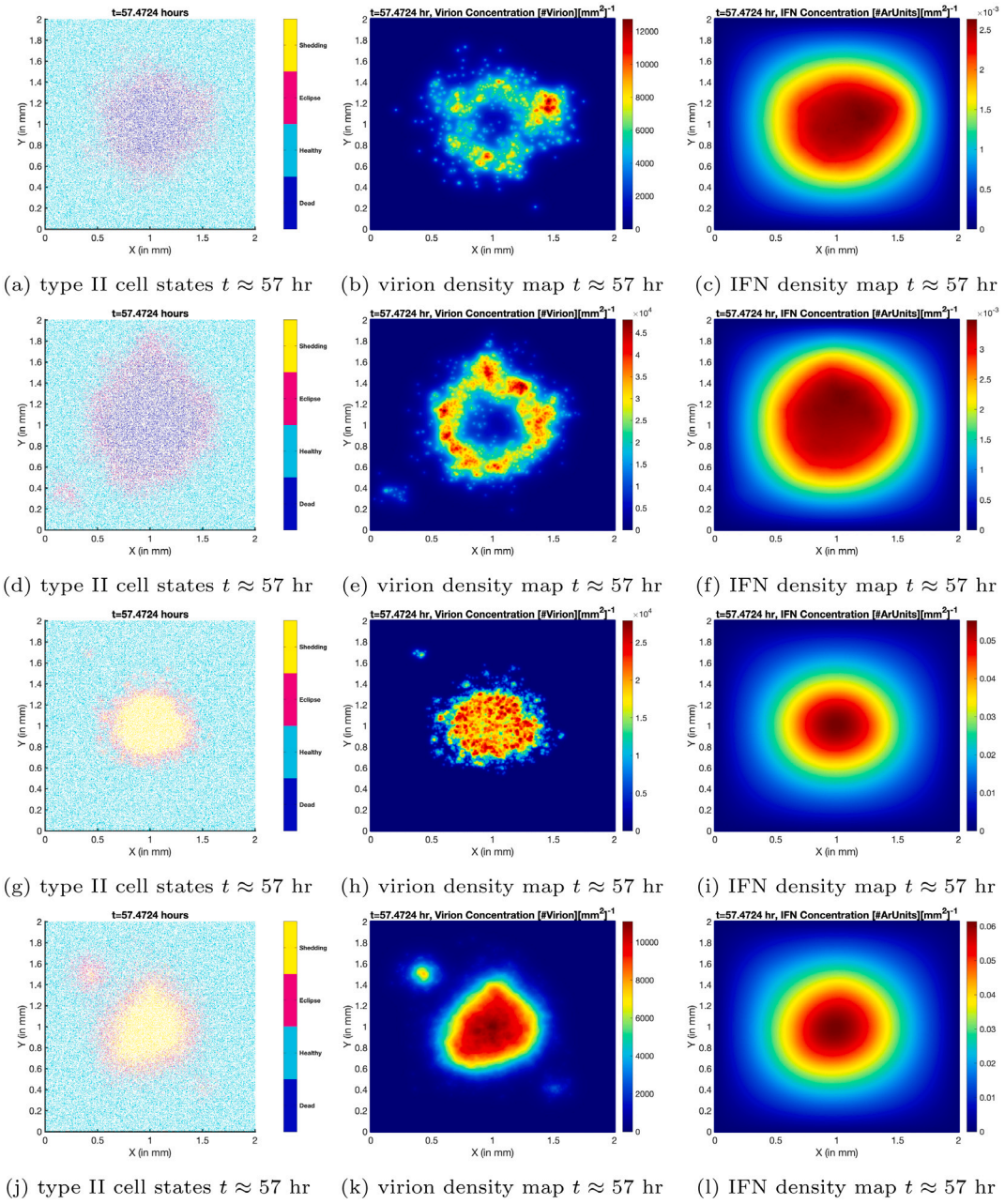

(a) type II cell states $t \approx 57$ hr (b) virion density map $t \approx 57$ hr (c) IFN density map $t \approx 57$ hr

(d) type II cell states $t \approx 57$ hr (e) virion density map $t \approx 57$ hr (f) IFN density map $t \approx 57$ hr

(g) type II cell states $t \approx 57$ hr (h) virion density map $t \approx 57$ hr (i) IFN density map $t \approx 57$ hr

(j) type II cell states $t \approx 57$ hr (k) virion density map $t \approx 57$ hr (l) IFN density map $t \approx 57$ hr

Fig. 7. Comparison of combined and individual IFN-induced innate immune mechanisms. Column 1 shows the type II cell states, Column 2 the virion density heatmaps, and Column 3 the IFN density heatmaps, all from snapshots at $t \approx 57$ h post infection of a single type II cell. Row 1 is with combined effects from immunity parameters $\delta = 1$, $\kappa = 1$, $u_c = 0.001$. Row 2 is with the single effect of macrophages and NK cell killing of infected type II cells with $\delta = 1$. Row 3 is with the single effect of macrophage killing of virions with $\kappa = 1$. Row 4 is with the single effect of suppressed replication and shedding of virions by infected cells with $u_c = 0.001$.

are turned on, when the entire domain becomes completely infected (see panel 8(a)) after around 100 h, see panel 8(d). Thus, the paracrine effect is an effective mechanism, as was shown in a recent work by other authors (Michael Lavigne et al., 2021). Now in Fig. 8-column 3 and specifically panel 8(c) we can see that after 142 h, all four IFN-mechanisms combined (including the paracrine effect) produce an infected area of similar size to the case where only the paracrine mechanism was on, in panel 8(b). Moreover the number of immunized cells in the combined case, panel 8(f), is approximately only one third of the number observed when there is no other IFN mechanism but the paracrine one, in panel 8(e). This again is attributed to the fact that in the combined case where immune cells are allowed to kill the infected type II cells, the level of IFN (see panel 8(o)) concentration is significantly lower than in panel 8(n), and this is the reason that a truly additive effect is not observed when all IFN-induced mechanisms are turned on. So in this case we also surmise that IFN produced by immune cells may be needed to properly maintain a high level of efficacy of the described IFN-dependent innate immunity mechanisms.

5. Conclusion

In this paper we developed a hybrid discrete stochastic-continuum PDE model for the evolution of spatially distributed SARS-CoV-2 infection in the lung parenchyma (alveolar space). The modeling platform superimposes four IFN-induced innate immune responses as well as antibody protection. For this paper, we focused simulations solely on the IFN signaling mechanisms of: suppression of assembly, replication, and shedding of virions by infected cells; signaling of macrophages

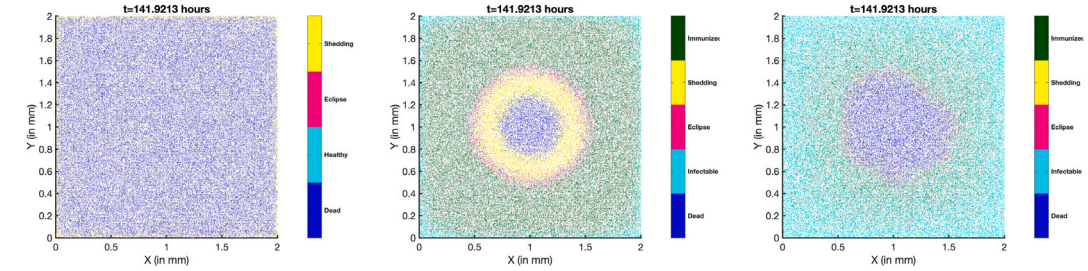

(a) type II cell states $t \approx 142$ hr (b) type II cell states $t \approx 142$ hr (c) type II cell states $t \approx 142$ hr

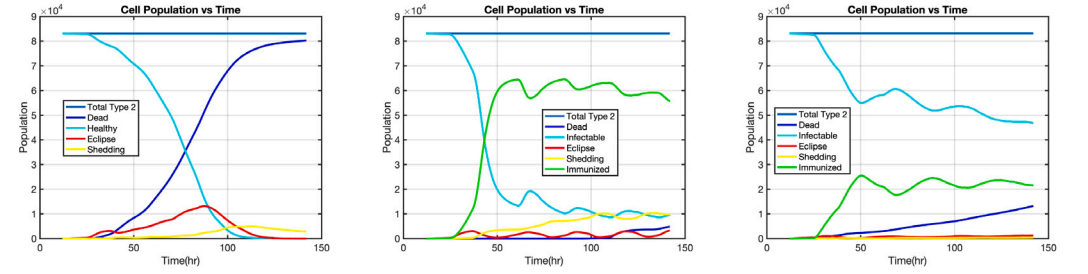

(d) cell state switching dynamics (e) cell state switching dynamics (f) cell state switching dynamics

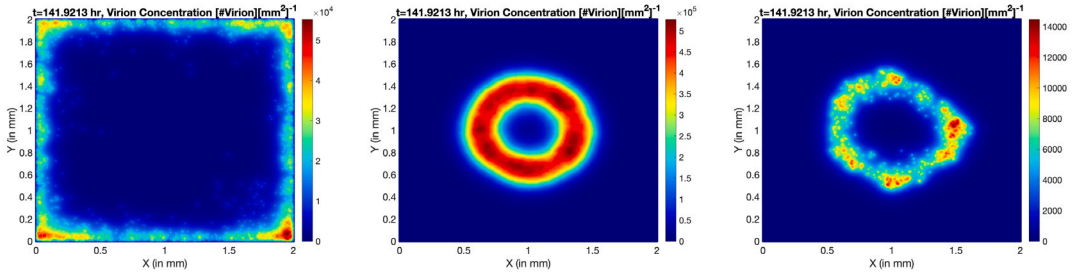

(g) virion density map $t \approx 142$ hr (h) virion density map $t \approx 142$ hr (i) virion density map $t \approx 142$ hr

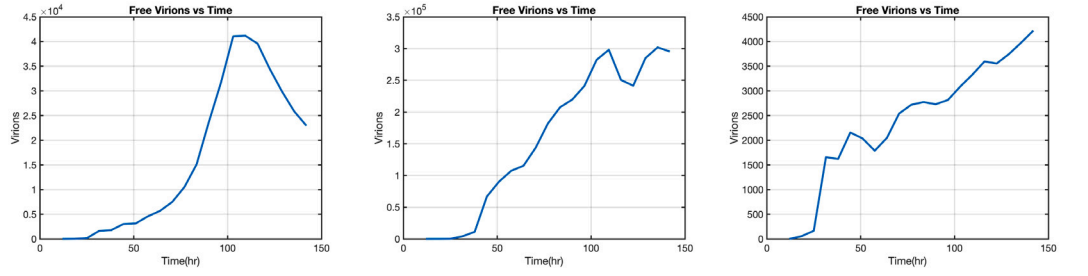

(j) total free virion dynamics (k) total free virion dynamics (l) total free virion dynamics

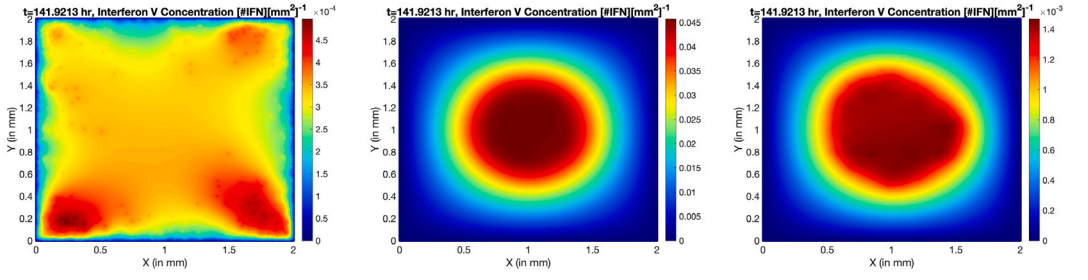

(m) IFN density map $t \approx 142$ hr (n) IFN density map $t \approx 142$ hr (o) IFN density map $t \approx 142$ hr

Fig. 8. Effects of IFN-induced paracrine effect. Column 1 has no paracrine mechanism, and it corresponds to the same case and parameters as in first row of Fig. 7 which features the first three combined IFN mechanisms. Column 2 corresponds to having only the fourth IFN mechanism, i.e., the paracrine effect, turned on with parameters $J = 0.01$ cell^{-1} min^{-1} [# IFN units]$^{-1}$ cm^2 and $\tau_4 = 24$ h. Column 2 features all four IFN-induced mechanisms turned on, combining the scenarios, and combining the same parameters, corresponding to the simulations in columns 1 and 2.

to eliminate virions; signaling of macrophages and natural killer cells to eliminate infected cells; and rendering of infectable cells refractory to viral infection. The model illustrates diverse outcomes from the degrees of protection that are possible by tuning the strength of each mechanism acting individually, and then one illustration each of the first three and all four mechanisms acting collectively. The model

output consists of the dynamic progression over the spatial lattice of type I (noninfectable) and type II (infectable) alveolar cells of (i) infected type II cells in the eclipse, shedding, (immunized) and death phases, (ii) virion concentration, and (iii) IFN concentration.

An interesting insight is gained from the presented simulation results. Namely, in our model the four IFN-induced mechanisms depend solely on IFN produced by infected type II alveolar cells. Our simulations suggest that within our modeling framework, the four mechanisms acting in concert do not produce an additive effect. Rather, the model predicts they collectively lead to progressively lower IFN levels as the infection is slowed, reducing the effectiveness against infection, a negative feedback effect. E.g., IFN-signaled macrophages or NK cells kill infected type II cells which no longer shed IFN, thus knocking down the other IFN-induced protections. A similar effect was observed in the context of influenza (Pawelek et al., 2012). We surmise that this result highlights the reason why the immune system evolved to build IFN, including type II IFN (Lee and Ashkar, 2018) – produced by immune cells – which recruit more immune cells, supplementing the function of the defense mechanism.

The modeling framework developed here is adaptable for the study of other pneumonia-causing viral pathogens (Torres et al., 2021), e.g., influenza, respiratory syncytial virus (RSV), human metapneumovirus (HMPV), rhinovirus. To do so, the SARS-CoV-2 transport and infection mechanisms are replaced by the virus of interest, similar to how we explored the mutational impacts on infection mechanisms of the SARS-CoV-2 variants (Pearson et al., 2022). With more physiological adaptations, we envision studying viral infections of other tissues, e.g., infection of the human cornea (Miner et al., 2020), where yet another type III class of IFN provides protection.

In future iterations of our alveolar infection model we plan to account for IFN produced by immune cells and to extend the model to adaptive immune protection (T cells). It is also worthwhile to explicitly incorporate immune cell species (macrophages, T cells, natural killer cells), although this will require detailed information about their IFN signaling and transport mechanics. A relatively easy application of this framework is to model inhaled deep lung delivery of monoclonal antibodies or antiviral drugs at any stage prior to or during active infections.

CRediT authorship contribution statement

Andreas C. Aristotelous: Conceived of the study, Analyzed, and interpreted the model simulations, Wrote all versions of the paper, Developed the model, Wrote the software, Performed the simulations. **Alex Chen:** Conceived of the study, Analyzed, and interpreted the model simulations, Wrote all versions of the paper. **M. Gregory Forest:** Conceived of the study, Analyzed, and interpreted the model simulations, Wrote all versions of the paper.

Declaration of competing interest

The authors declare that they have no known competing financial interests or personal relationships that could have appeared to influence the work reported in this paper.

Data availability

The code generated the data is not stand-alone to share, since is a part of a larger software package developed by ACA that he plans to publish as a separate publication linking all relevant works.

Acknowledgment

The authors would like to thank the anonymous referees for valuable comments, information, suggestions and references that contributed to the final version of this paper.

References

Aristotelous, A.C., Durrett, R., 2014a. Chemical evolutionary games. Theor. Popul. Biol. 93, 1–13.

Aristotelous, A.C., Durrett, R., 2014b. Fingering in stochastic growth models. Experiment. Math. 23 (4), 465–474. http://dx.doi.org/10.1080/10586458.2014.947053.

Bar-On, Y.M., Flamholz, A., Phillips, R., Milo, R., 2020. Science Forum: SARS-CoV-2 (COVID-19) by the numbers. ELIfe 9, e57309.

Blot, M., Jacquier, M., Manoha, C., Piroth, L., Charles, P.-E., 2021. Alveolar SARS-CoV-2 viral load is tightly correlated with severity in COVID-19 ARDS. Clin. Infect. Dis. 72 (9), e446–e447.

Bost, P., Giladi, A., Liu, Y., Bendjelal, Y., Xu, G., David, E., Blecher-Gonen, R., Cohen, M., Medaglia, C., Li, H., et al., 2020. Host-viral infection maps reveal signatures of severe COVID-19 patients. Cell 181 (7), 1475–1488.

Chen, A., Wessler, T., Daftari, K., Hinton, K., Boucher, R.C., Pickles, R., Freeman, R., Lai, S.K., Forest, M.G., 2022a. Modeling insights into SARS-CoV-2 respiratory tract infections prior to immune protection. Biophys. J. 121 (9), 1619–1631.

Chen, A., Wessler, T., Forest, M.G., 2022b. Antibody protection from SARS-CoV-2 respiratory tract exposure and infection. Submitt. J. Theor. Biol..

Cummings, K.W., Levy, D.N., Wodarz, D., 2012. Increased burst size in multiply infected cells can alter basic virus dynamics. Biol. Dir. 7 (1), 16. http://dx.doi.org/10.1186/1745-6150-7-16.

Davis, T.A., 2006. Direct Methods for Sparse Linear Systems. Society for Industrial and Applied Mathematics, 3600 University City Science Center, Philadelphia, PA, United States, http://dx.doi.org/10.1137/1.9780898718881.

Dinnon, K.H., Leist, S.R., Schäfer, A., Edwards, C.E., Martinez, D.R., Montgomery, S.A., West, A., Yount, B.L., Hou, Y.J., Adams, L.E., Gully, K.L., Brown, A.J., Huang, E., Bryant, M.D., Choong, I.C., Glenn, J.S., Gralinski, L.E., Sheahan, T.P., Baric, R.S., 2020. A mouse-adapted model of SARS-CoV-2 to test COVID-19 countermeasures. Nature 586 (7830), 560–566. http://dx.doi.org/10.1038/s41586-020-2708-8.

Domingo-Calap, P., Segredo-Otero, E., Durán-Moreno, M., Sanjuán, R., 2019. Social evolution of innate immunity evasion in a virus. Nat. Microbiol. 4 (6), 1006–1013. http://dx.doi.org/10.1038/s41564-019-0379-8.

Gattinoni, L., Coppola, S., Cressoni, M., Busana, M., Rossi, S., Chiumello, D., 2020. COVID-19 does not lead to a "typical" acute respiratory distress syndrome. Am. J. Respir. Crit. Care Med. 201 (10), 1299–1300.

Goyal, A., Duke, E.R., Cardozo-Ojeda, E.F., Schiffer, J.T., 2022. Modeling explains prolonged SARS-CoV-2 nasal shedding relative to lung shedding in remdesivir-treated rhesus macaques. IScience 25 (6), http://dx.doi.org/10.1016/j.isci.2022.104448.

Grant, R.A., Morales-Nebreda, L., Markov, N.S., Swaminathan, S., Querrey, M., Guzman, E.R., Abbott, D.A., Donnelly, H.K., Donayre, A., Goldberg, I.A., et al., 2021. Circuits between infected macrophages and T cells in SARS-CoV-2 pneumonia. Nature 590 (7847), 635–641.

Hagemann, K., Riecken, K., Jung, J.M., Hildebrandt, H., Menzel, S., Bunders, M.J., Fehse, B., Koch-Nolte, F., Heinrich, F., Peine, S., et al., 2022. Natural killer cell-mediated ADCC in SARS-CoV-2-infected individuals and vaccine recipients. Eur. J. Immunol..

Hou, Y.J., Okuda, K., Edwards, C.E., Martinez, D.R., Asakura, T., Dinnon III, K.H., Kato, T., Lee, R.E., Yount, B.L., Mascenik, T.M., Chen, G., Olivier, K.N., Ghio, A., Tse, L.V., Leist, S.R., Gralinski, L.E., Schäfer, A., Dang, H., Gilmore, R., Nakano, S., Sun, L., Fulcher, M.L., Livraghi-Butrico, A., Nicely, N.I., Cameron, M., Cameron, C., Kelvin, D.J., de Silva, A., Margolis, D.M., Markmann, A., Bartelt, L., Zumwalt, R., Martinez, F.J., Salvatore, S.P., Borczuk, A., Tata, P.R., Sontake, V., Kimple, A., Jaspers, I., O'Neal, W.K., Randell, S.H., Boucher, R.C., Baric, R.S., 2020. SARS-CoV-2 reverse genetics reveals a variable infection gradient in the respiratory tract. Cell 182 (2), 429–446.e14. http://dx.doi.org/10.1016/j.cell.2020.05.042.

Hui, K.P., Ho, J.C., Cheung, M.-c., Ng, K.-c., Ching, R.H., Lai, K.-l., Kam, T.T., Gu, H., Sit, K.-Y., Hsin, M.K., et al., 2022. SARS-CoV-2 Omicron variant replication in human bronchus and lung ex vivo. Nature 603 (7902), 715–720.

Iyer, S.S., Bibollet-Ruche, F., Sherrill-Mix, S., Learn, G.H., Plenderleith, L., Smith, A.G., Barbian, H.J., Russell, R.M., Gondim, M.V.P., Bahari, C.Y., Shaw, C.M., Li, Y., Decker, T., Haynes, B.F., Shaw, G.M., Sharp, P.M., Borrow, P., Hahn, B.H., 2017. Resistance to type 1 interferons is a major determinant of HIV-1 transmission fitness. Proc. Natl. Acad. Sci. 114 (4), E590–E599. http://dx.doi.org/10.1073/pnas.1620144114, arXiv:https://www.pnas.org/doi/pdf/10.1073/pnas.1620144114 URL https://www.pnas.org/doi/abs/10.1073/pnas.1620144114.

Janeway, C.A., Travers, P., Walport, M., Capra, D.J., 2001. Immunobiology. Garland Science, Taylor & Francis Group UK.

Jung, C., Kmiec, D., Koepke, L., Zech, F., Jacob, T., Sparrer, K.M., Kirchhoff, F., 2022. Omicron: what makes the latest SARS-CoV-2 variant of concern so concerning? J. Virol. 96 (6), e02077–21.

Ke, R., Zitzmann, C., Ho, D.D., Ribeiro, R.M., Perelson, A.S., 2021. In vivo kinetics of SARS-CoV-2 infection and its relationship with a person's infectiousness. Proceedings of the National Academy of Sciences 118 (49), http://dx.doi.org/10.1073/pnas.2111477118, e2111477118.

Kissler, S.M., Fauver, J.R., Mack, C., Olesen, S.W., Tai, C., Shiue, K.Y., Kalinich, C.C., Jednak, S., Ott, I.M., Vogels, C.B., et al., 2021. Viral dynamics of acute SARS-CoV-2 infection and applications to diagnostic and public health strategies. PLoS Comput. Biol. 19 (7), e3001333.

Korber, B., Fischer, W.M., Gnanakaran, S., Yoon, H., Theiler, J., Abfalterer, W., Hengartner, N., Giorgi, E.E., Bhattacharya, T., Foley, B., et al., 2020. Tracking changes in SARS-CoV-2 spike: evidence that D614G increases infectivity of the COVID-19 virus. Cell 182 (4), 812–827.

Kreuz, L.E., Levy, A.H., 1965. Physical properties of chick interferon. J. Bacteriol. 89 (2), 462–469. http://dx.doi.org/10.1128/jb.89.2.462-469.1965.

Lai, S.K., Hida, K., Shukair, S., Wang, Y.-Y., Figueiredo, A., Cone, R., Hope, T.J., Hanes, J., 2009. Human immunodeficiency virus type 1 is trapped by acidic but not by neutralized human cervicovaginal mucus. J. Virol. 83 (21), 11196–11200.

Lamers, M.M., Haagmans, B.L., 2022. SARS-CoV-2 pathogenesis. Nat. Rev. Microbio. 20 (5), 270–284.

Lee, A.J., Ashkar, A.A., 2018. The dual nature of type I and type II interferons. Front. Immunol. 9, http://dx.doi.org/10.3389/fimmu.2018.02061.

Liggett, T.M., 1985. Interacting Particle Systems. Springer-Verlag, New York, NY.

Liu, C.-S., Atluri, S.N., 2008. A novel time integration method for solving a large system of non-linear algebraic equations. CMES Comput. Model. Eng. Sci. 31 (2), 71–84. http://dx.doi.org/10.3970/cmes.2008.031.071.

Liu, S.-Y., Sanchez, D.J., Aliyari, R., Lu, S., Cheng, G., 2012. Systematic identification of type I and type II interferon-induced antiviral factors. Proc. Natl. Acad. Sci. 109 (11), 4239–4244. http://dx.doi.org/10.1073/pnas.1114981109.

Lv, J., Wang, Z., Qu, Y., Zhu, H., Zhu, Q., Tong, W., Bao, L., Lv, Q., Cong, J., Li, D., et al., 2021. Distinct uptake, amplification, and release of SARS-CoV-2 by M1 and M2 alveolar macrophages. Cell Discov. 7 (1), 1–12.

Mantlo, E., Bukreyeva, N., Maruyama, J., Paessler, S., Huang, C., 2020. Antiviral activities of type I interferons to SARS-CoV-2 infection. Antiviral Res. 179, 104811. http://dx.doi.org/10.1016/j.antiviral.2020.104811.

McNab, F., Mayer-Barber, K., Sher, A., Wack, A., O'garra, A., 2015. Type I interferons in infectious disease. Nat. Rev. Immunol. 15 (2), 87–103.

Michael Lavigne, G., Hayley, R., Barbara, S., Ruian, K., 2021. Autocrine and paracrine interferon signalling as 'ring vaccination' and 'contact tracing' strategies to suppress virus infection in a host. Proc. R. Soc. B. 288, http://dx.doi.org/10.1098/rspb.2020.3002.

Miner, J.J., Platt, D.J., Ghaznavi, C.M., Chandra, P., Santeford, A., Menos, A.M., Dong, Z., Wang, E.R., Qian, W., Karozichian, E.S., Philips, J.A., Apte, R.S., 2020. HSV-1 and zika virus but not SARS-CoV-2 replicate in the human cornea and are restricted by corneal type III interferon. Cell Rep. 33 (5), 108339. http://dx.doi.org/10.1016/j.celrep.2020.108339.

Moses, M.E., Hofmeyr, S., Cannon, J.L., Andrews, A., Gridley, R., Hinga, M., Leyba, K., Pribisova, A., Surjadidjaja, V., Tasnim, H., et al., 2021. Spatially distributed infection increases viral load in a computational model of SARS-CoV-2 lung infection. PLoS Comput. Biol. 17 (12), e1009735.

Olmsted, S.S., Padgett, J.L., Yudin, A.I., Whaley, K.J., Moench, T.R., Cone, R.A., 2001. Diffusion of macromolecules and virus-like particles in human cervical mucus. Biophys. J. 81 (4), 1930–1937.

Park, B.K., Kim, D., Park, S., Maharjan, S., Kim, J., Choi, J.-K., Akauliya, M., Lee, Y., Kwon, H.-J., 2021. Differential signaling and virus production in Calu-3 cells and Vero cells upon SARS-CoV-2 infection. Biomol. Ther. 29 (3), 273.

Pawelek, K.A., Huynh, G.T., Quinlivan, M., Cullinane, A., Rong, L., Perelson, A.S., 2012. Modeling within-host dynamics of influenza virus infection including immune responses. PLoS Comput. Biol. 8 (6), e1002588.

Peacock, T.P., Brown, J.C., Zhou, J., Thakur, N., Newman, J., Kugathasan, R., Sukhova, K., Kaforou, M., Bailey, D., Barclay, W.S., 2022. The SARS-CoV-2 variant, Omicron, shows rapid replication in human primary nasal epithelial cultures and efficiently uses the endosomal route of entry. http://dx.doi.org/10.1101/2021.12.31.474653, BioRxiv.

Pearson, J.E.A., Krapivsky, P.A., Perelson, A.S., 2011. Stochastic theory of early viral infection: Continuous versus burst production of virions. PLoS Comput. Biol. 7 (2), 1–17. http://dx.doi.org/10.1371/journal.pcbi.1001058.

Pearson, J., Wessler, T., Chen, A., Boucher, R.C., Freeman, R., Lai, S.K., Pickles, R., Forest, M.G., 2022. A mechanistic explanation for ballistic rises in nasal infections of the SARS-CoV-2 variants. Preprint.

Richardson, D., 1973. Random growth in a tesselation. Proc. Camb. Phil. Soc. 74, 515–528.

Sa Ribero, M., Jouvenet, N., Dreux, M., Nisole, S., 2020. Interplay between SARS-CoV-2 and the type I interferon response. PLOS Pathogens 16 (7), 1–22. http://dx.doi.org/10.1371/journal.ppat.1008737.

Sallard, E., Lescure, F.-X., Yazdanpanah, Y., Mentre, F., Peiffer-Smadja, N., 2020. Type 1 interferons as a potential treatment against COVID-19. Antiviral Res. 178, 104791.

Saltzman, W.M., Radomsky, M.L., Whaley, K.J., Cone, R.A., 1994. Antibody diffusion in human cervical mucus. Biophys. J. 66 (2), 508–515.

Segredo-Otero, E., Sanjuán, R., 2020. The role of spatial structure in the evolution of viral innate immunity evasion: A diffusion-reaction cellular automaton model. PLoS Comput. Biol. 16 (2), e1007656.

Sender, R., Bar-On, Y.M., Gleizer, S., Bernshtein, B., Flamholz, A., Phillips, R., Milo, R., 2021. The total number and mass of SARS-CoV-2 virions. Proc. Natl. Acad. Sci. 118 (25), e2024815118.

Smither, S.J., Eastaugh, L.S., Findlay, J.S., Lever, M.S., 2020. Experimental aerosol survival of SARS-CoV-2 in artificial saliva and tissue culture media at medium and high humidity. Emerg. Microbes Infect. 9 (1), 1415–1417. http://dx.doi.org/10.1080/22221751.2020.1777906, PMID: 32496967.

Swiecki, M., Colonna, M., 2011. Type I interferons: diversity of sources, production pathways and effects on immune responses. Curr. Opin. Virol. 1 (6), 463–475. http://dx.doi.org/10.1016/j.coviro.2011.10.026, URL https://www.sciencedirect.com/science/article/pii/S187962571100160X. Innate immunity/Antivirals and resistance/Emerging viruses.

Torres, A., Cilloniz, C., Niederman, M.S., Menéndez, R., Chalmers, J.D., Wunderink, R.G., van der Poll, T., 2021. Pneumonia. Nat. Rev. Dis. Primers 7 (1), 25. http://dx.doi.org/10.1038/s41572-021-00259-0.

Vaidya, N.K., Bloomquist, A., Perelson, A.S., 2021. Modeling within-host dynamics of SARS-CoV-2 infection: A case study in ferrets. Viruses 13 (8), http://dx.doi.org/10.3390/v13081635, URL https://www.mdpi.com/1999-4915/13/8/1635.

Voigt, E.A., Swick, A., Yin, J., 2016. Rapid induction and persistence of paracrine-induced cellular antiviral states arrest viral infection spread in A549 cells. Virology 496, 59–66. http://dx.doi.org/10.1016/j.virol.2016.05.019, URL https://www.sciencedirect.com/science/article/pii/S0042682216301283.

Wang, J., Oberley-Deegan, R., Wang, S., Nikrad, M., Funk, C.J., Hartshorn, K.L., Mason, R.J., 2009. Differentiated human alveolar type II cells secrete antiviral IL-29 (IFN-λ1) in response to influenza A infection. J. Immunol. 182 (3), 1296–1304. http://dx.doi.org/10.4049/jimmunol.182.3.1296, arXiv:https://www.jimmunol.org/content/182/3/1296.full.pdf URL https://www.jimmunol.org/content/182/3/1296.

Wölfel, R., Corman, V.M., Guggemos, W., Seilmaier, M., Zange, S., Müller, M.A., Niemeyer, D., Jones, T.C., Vollmar, P., Rothe, C., et al., 2020. Virological assessment of hospitalized patients with COVID-2019. Nature 581 (7809), 465–469.

Zhou, F., Yu, T., Du, R., Fan, G., Liu, Y., Liu, Z., Xiang, J., Wang, Y., Song, B., Gu, X., et al., 2020. Clinical course and risk factors for mortality of adult inpatients with COVID-19 in Wuhan, China: a retrospective cohort study. Lancet 395 (10229), 1054–1062.